LUND UNIVERSITY
Faculty of Science

The production of samarium-cobalt nanoparticles using a spark discharge generator

Timothy Lewis

Thesis submitted for the degree of Master of Science
Project duration: 4 months

Supervised by Maria Messing and Calle Preger

Department of Physics
Division of Solid State Physics
May 2019

Abstract

In this project I attempt to press custom electrodes from Sm and Co powder using two different pressing tools. I investigate if custom electrodes can generate nanoparticles with tailored properties using a spark discharge generator (SDG). Three different sources of the nanoparticle material will be considered, pressed Sm and Co powder, pure Sm and Co electrodes and alloyed SmCo made from demagnetized magnets. The nanoparticles produced were analysed using tandem DMA to investigate the size distribution, concentration, thermal charging and oxidation of the particles. The particles were compacted and deposited using an ESP so that SEM analysis could be performed to examine the morphology and TEM/EDX to learn about the particle's elemental composition. The production of pressed SmCo electrodes was unsuccessful, but stainless steel electrodes were pressed, and it is hoped that custom electrodes can be produced using an improved tool. Compositional analysis of SmCo particles made from pure Sm and Co and alloyed electrodes both contained Sm and Co, but the internal elemental composition and morphology differed. The ability to produce nanoparticles with desirable properties using an SDG is good. Nanoparticles with tailored properties have potential to be generated and have a number of important applications in biomedicine.

Acronyms and Abbreviations

DMA	differential mobility analyser
EDX	energy-dispersive X-ray spectroscopy
ESP	electrostatic precipitator
MRI	magnetic resonance imaging
NP	nanoparticle
RT	room temperature
SDG	spark discharge generator
SEM	scanning electron microscope
SS	stainless steel
TEM	transmission electron microscope

Acknowledgements

Firstly, I would like to give my sincerest gratitude to Maria Messing for allowing me to participate in this project. For her patience to read my thesis and the guidance she gave me will be of great importance for my future career. In addition, I would like to thank Calle Preger who put in considerable time and effort to teach me how to use the SDG machine, SEM and answered every silly question I had. Calle gave me lots of feedback on the thesis managing to decipher my sentences and helped transform them into coherent points. I would also like to thank Bengt Mueller for ensuring that everything I did was safe in the department. I would like to thank the members of the Aerosol group Sara Thorberg, Markus Snellman and Namsoon Eom for their insightful comments and discussion during the process of writing this thesis.

Contents

Chapter 1

Introduction

Nanoscience and technology is an evolving field of research that has the potential to change the lives of people all around the world. Nanotechnology describes structures on the scale of a nanometer which is one billionth of a meter, a size comparable to that of atoms and molecules. Structures on this scale are interesting because they gain properties that are otherwise impossible for larger objects. Innovations as a result of Nanoscience have already been implemented in a number of consumer devices such as in electronics [1], air and water filtration systems [2] and medical devices. The ability to manipulate particles on the atomic level has had and will continue to have an impact on the world.

A common type of structure utilised in many different areas of nanoscience is the nanoparticle. Nanoparticles have quantum mechanical properties because they are small enough to confine their electrons. Nanoparticles also have a high surface to volume ratio which gives rise to high rates of diffusion, enabling nanoparticles to be suitable for an array of applications. Nanoparticles are an area of intense research and scientific interest as they can provide a link between bulk materials and the tiny atomic structures [3].

1.1 Nanoparticles

Nanoparticles surround us everywhere in the world today. Nanoparticles can be generated from many different natural sources such as the particles released in volcanic eruptions, the fine dust in desert storms and bacteria which break down compounds into biological nanoparticles [4]. Nanoparticles have a major effect on the environment, from the scale of the planet's climate to nanoparticles in the air that enter the human body. It has been shown that nanoparticles can help to reduce the effects of climate change by scattering incoming solar radiation to reduce the effects of greenhouse gases released by human activity [5]. Despite these potentially positive effects there are also a number of well established negative effects on human health. Elongated nanoparticles such as fibres are more dangerous than spherical particles and can penetrate deep into the lungs causing lung cancers and cardiopulmonary diseases [6]. Nanoparticle safety is of paramount importance and should not be underestimated when working with certain types of these potentially dangerous particles. The impact of nanoparticles is still being studied in the long term, however there is already significant evidence that certain kinds of nanoparticles are hazardous to human health.

Nanoparticles can be a vague term as nanoparticles can vary in size, shape and structure and technically can be used to refer to particles from 1 - 100 nm in size. Nanoparticles in the environment that are suspended in a gas are commonly referred to as aerosol nanoparticles [7]. In this thesis aerosol nanoparticles in the range of 1 - 200 nm will be addressed [8].

1.2 Aerosol Science

Aerosol technology has enabled interest in nanoparticles to increase rapidly over the past decades. It has opened up entirely new and exciting areas of research using nanoparticles that were previously impossible due to the lack of technology. There are many natural sources of aerosol nanoparticles, however many of these processes have limitations. The production of the nanoparticles cannot be controlled so the nanoparticles are often not as pure, not material independent and their size cannot be accurately adjusted. But in recent history the tools and techniques have become available that allow for the creation of particles on the scale of nanometers. The work in this thesis covers nanoparticles that were produced using a plasma-based aerosol method of production called spark discharge generation [8]. The generation of nanoparticles is a significant milestone for the field of aerosol science and will continue to be at the forefront of the field.

Aerosol nanoparticle generators are devices which allow a user to generate nanoparticles suspended in a gas flow. These devices have a number of strengths that make them a favourable method for performing research on engineered nanoparticles. The device allows for quick control of the size of the particles and the composition with alterations being possible in flight. The production is a fast process and allows for continuous production of the nanoparticles allowing iterative steps to be taken to improve the output. The nanoparticles can be studied in more flexible ways compared to many other production methods of nanoparticles. Aerosol-based production methods also have the ability to deposit particles onto solid structures without additional chemicals. This could allow for the ability to construct complex structures from nanoparticles [9]. Spark discharge generation is a particularly good method for forming complex alloys as the plasma-based technique mixes metallic elements on the atomic level. This is an important ability because it is highly probable that nanoparticles with desirable properties will be a combination of metallic elements [10]. The majority of elements in the periodic table are metallic and combinations of these elements make thousands of possible candidates. If nanoparticles are required that need to react under magnetic fields in a specific way or catalyse a reaction it is likely that the composition of the nanoparticle will be bimetallic.

1.3 Engineered Nanoparticles

The capabilities of engineered multielement nanoparticles have improved rapidly over the past years. In March 2018 in the cover article of the journal Science, researchers showed that it was possible to combine multiple metals into nanoparticles, including many not thought to be able to mix [11]. It has only recently been possible to deposit nanoparticles into complex arrays of 3D nanostructures [12]. Another type of engineered nanoparticle that has shown significant progress is in the synthesis of magnetic nanoparticles. Biomedical applications are of particular interest because of the particles unique ability to be

used as a guided drug carrier in the body or as contrast agents for magnetic resonance imaging (MRI) [13]. However more research is needed into how magnetic nanoparticles with desirable properties can be produced.

Different nanoparticle applications require a range of different manufacturing processes. Nanoparticles produced from organic non-toxic polymers are often used for biomedical applications, whereas nanoparticles used for electronic applications can be produced from a range of mechanical or chemical processes. The research performed on magnetic nanoparticle has mostly been performed on nanoparticles synthesised via chemical processes. Chemical processes have a number of advantages and disadvantages which may not make them best suited to research into magnetic nanoparticles. Chemical synthesis of nanoparticles relies on the use of chemical precursors and solvents in the liquid or gas phase. These chemical components can be expensive and are single use which can result in impure nanoparticles that do not exhibit the properties you wish to study. The production of aerosol magnetic nanoparticles is still not well known and further knowledge is needed [14].

Magnetic nanoparticles can be carefully controlled with magnetic fields at distances to move them into places that are inaccessible to larger particles [15]. Medical applications such as experimental cancer treatments by heating up nanoparticles to destroy cancer cells are being researched. As well as applications as catalytic supports to promote favourable reaction pathways and create greater yields. One important challenge of nanoscience research is the production of nanoparticles with tailored properties that are synthesised from complex materials. This thesis will research which methods are effective to create nanoparticles from an alloy of metallic materials in an attempt to create tailored nanoparticles with potentially magnetic properties. This thesis will investigate three production methods for creating samarium-cobalt nanoparticles.

1.4 Thesis Description

I have studied and investigated the production of nanoparticles from magnetic composite materials using a spark discharge generator (SDG). There is a demand for new production methods of nanoparticles that are tunable and can produce nanoparticles with tailored properties. The aerosol production method using a spark discharge generator is a good candidate, the machine creates a spark between electrodes that gives control over several important parameters. The aim of the project was to investigate the effect of the electrode type on the generated nanoparticles, a topic that is not well studied. The project consists of three main parts. The first part is to investigate if it is possible to manufacture pure samarium-cobalt electrodes from powder. The second part of the project is to produce samarium-cobalt nanoparticles from different sources to consider if it is possible to make nanoparticles with desirable properties. The three different sources of nanoparticles will be alloyed samarium-cobalt as used in commercially available magnets, two electrodes of pure samarium and pure cobalt and the pressed electrodes of samarium-cobalt. In the final part of the project I will analyse the nanoparticles to compare the differences in production and to understand which method is the best candidate to produce potentially magnetic nanoparticles.

1.4.1 Thesis outline

Chapter 2: Aerosol Physics. This chapter describes the concepts of aerosol physics that are important for this project. What defines nanoparticles, the role of magnetism in magnetic nanoparticles and the motion of these particles in the aerosol phase.

Chapter 3: Electrodes, NP Synthesis and Analysis. This chapter describes how nanoparticles are created and analysed. A description of the machine and how it was used to create the particles. A summary of the different stages and states of particle formation during the synthesis. A brief summary of the different relevant techniques for the analysis of the nanoparticles in this thesis.

Chapter 4: Pressed Samarium-Cobalt Electrodes. This chapter will present the results of the manufacturing of custom electrodes for particle creation. The results will be discussed to evaluate the potential of pressing custom electrodes.

Chapter 5: Samarium-Cobalt Nanoparticle Analysis. This chapter will present the results of the different methods of producing samarium-cobalt nanoparticles. The results will be discussed with reference to previous studies to evaluate the different electrode types.

Chapter 6: Outlook and Conclusion. This chapter will be the concluding thoughts of the project and an outlook on future research relevant to this thesis.

Chapter 2

Aerosol Physics

Aerosol technology has developed into a broad and diverse field that tackles a range of problems facing society today. From problems on the scale of the planet to the challenges of protecting the earth against the polluting particles released into the environment every single day. Aerosols are defined in there most basic form as solid or liquid particles that are suspended in a gas. This is an ambiguous definition and could be applied to a number of completely unrelated research areas. However, the shared pillar of aerosol physics is the instruments that characterise the particles and so aerosol particles are in the range of 1 nm up to 1 mm in diameter. The particles in an aerosol system can be understood and controlled in specific ways since the production of particles in the system is guided from the source to the output. It is a natural consequence that to understand the nanoparticle production we need to have a good understanding of the underlying physics that drives the production.

Aerosol nanoparticles generation is a powerful and flexible tool. Generating aerosol nanoparticles is a very controllable process as the particles are transported by a carrier gas. The particles can be measured and changed in the system as they move in the system. To understand the way that nanoparticles move in a carrier gas aerosol system requires fundamental knowledge of aerosol physics which help to understand how nanoparticles are generated. In this chapter the important physics of aerosols relevant to this thesis will be presented. An important reference for the theory in this thesis is the book, "Aerosol Technology: properties, behaviour, and measurement of airborne particles" by Hinds [7].

2.1 Nanoparticle Mobility

Aerosols are two phase systems which refer to both the particles and the carrier gas which the particles are suspended in. Nanoparticles can have different stabilities and sizes and will move differently in gases of varying viscosities. These parameters are essential to understanding how the particles will move in an aerosol system. The two types of flows are laminar and turbulent flow which can be seen in Figure 2.1 below along with each regimes range of Reynolds number Re. Laminar flow is sheet-like flow in which a particle moves parallel to the transport medium with little to no disruption between the layers of the medium. In contrast turbulent flow is characterised by chaotic motion with rapid changes in the transport medium. The Reynolds number is a way to determine if a particle will move in a laminar or turbulent motion in a gas flow. The Reynolds number is given by equation 2.1 where ρ is the density of the carrier gas, V is the volume, d is the particle

diameter and η is the velocity of the gas.

$$Re = \frac{\rho V d}{\eta} \tag{2.1}$$

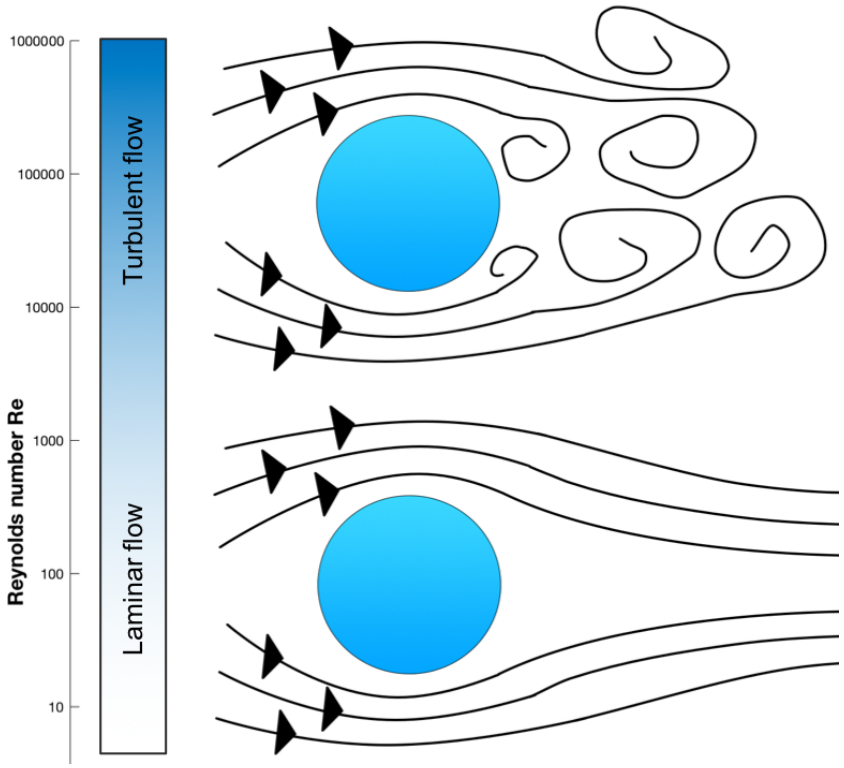

Figure 2.1: Illustration of a particle in both laminar and turbulent flow regimes with the range of Reynolds number for each type of flow.

The nanoparticles created in this thesis move at high velocities in the gas flow which is contained in a narrow tube. The particles have very low mass and inertia and in combination with the high-velocity flow results in a very small Reynolds number of less than one. Therefore the nanoparticles in this thesis will move in a laminar flow. However, the narrow tubes in the system give rise to resistive forces which can have a big impact on the type of flow in the channel. The resistive or drag forces F_d are given by Stokes law in equation 2.2 where v is the flow velocity.

$$F_d = 3\pi\eta v d \tag{2.2}$$

Nanoparticles have very low mass and so gravitational forces can be ignored, the dominant forces are Brownian forces. These forces are the result of random collisions with gas molecules and are the dominant force on nanoparticles in gas flows characterised by a low Reynolds number. Another factor to consider is that as the size of particles decrease the simplifications made as a part of Stokes law become less and less true. This simplification is to assume the relative velocity between the particles surface and gas is zero. However, small particles whose size is similar to the mean free path λ, particles of sizes smaller than 100 nm have a decreased drag force [16]. This is because smaller particles have an increased chance of avoiding collisions with gas molecules by slipping away. The decrease

in drag force can be taken into account by introducing the Cunningham correction factor C_c which is given by equation 2.3.

$$C_c = 1 + \frac{\lambda}{d}[2.34 + 1.05exp(-0.39\frac{d}{\lambda})] \tag{2.3}$$

The Cunningham correction factor is always bigger than one and so reduces the drag force, it becomes an important factor as particles decrease in size. The drag force in Stokes law is divided by the Cunningham correction factor as shown in equation 2.4.

$$F_D = \frac{3\pi\eta v d_p}{C_c} \tag{2.4}$$

2.2 Differential Mobility Analyser (DMA)

One of the strengths of aerosol nanoparticle production is the ability to control the size of particles. In order to understand how the size of particles change the system needs to be able to size select particles. Particles are size selected in the aerosol system using a differential mobility analyser (DMA) which selects particles based on their electrical mobility Z. This parameter determines how much a particle moves in the presence of an electric field and is given by equation 2.5, where n is the number of charges on the particle e is the elementary charge of the electron, C_c is the Cunningham correction factor, d_p is the particle diameter and η is the viscosity of the carrier gas.

$$Z = \frac{neC_c}{3\pi\eta d_p} \tag{2.5}$$

It can be seen in equation 2.5 that particles of the same charge, contained in the same carrier gas can have their diameters distinguished by their electrical mobility. The DMA first uses an impactor to remove very large particles over 10 μm, these particles can cause problems in the DMA functions. The incoming aerosol is given a known charge distribution and then injected between two capacitor plates which generate an electric field causing the aerosol to be accelerated. A laminar flow of carrier gas carries the fraction of nanoparticles with the desired mobility towards an exit slit. Small particles that have too large electrical mobility Z are accelerated by the electric field impact, reaching the capacitor plate. Large particles with too small electrical mobility as well as uncharged particles are carried away by the sheath flow gas. A diagram showing how a DMA operates to select particles based on electrical mobility is shown below in Figure 2.2.

A DMA classifies and measures aerosol nanoparticles based on their size however the diameter d_p of the particles should not be confused for the mobility diameter Z. For singly charged particles that have a spherical shape the DMA works well as the geometric size is equal to the mobility size. However, many particles have a chain like structure or multiple charges which can be more difficult to identify accurately and require greater interpretation of the data. There are also additional errors in the fraction of nanoparticles that are selected ΔZ. These errors arise from several sources one of the most important is because the exit slit of the DMA seen in Figure 2.2 has a finite width. The random, Brownian motion of the particles will reduce the performance of the DMA as well as diffusion broadening. The parameter which defines a DMA performance is its transfer function $\Omega(Z, Z*)$ this is the probability that a particle with electrical mobility Z will go through a DMA that has been set to identify particles with mobility Z* [16].

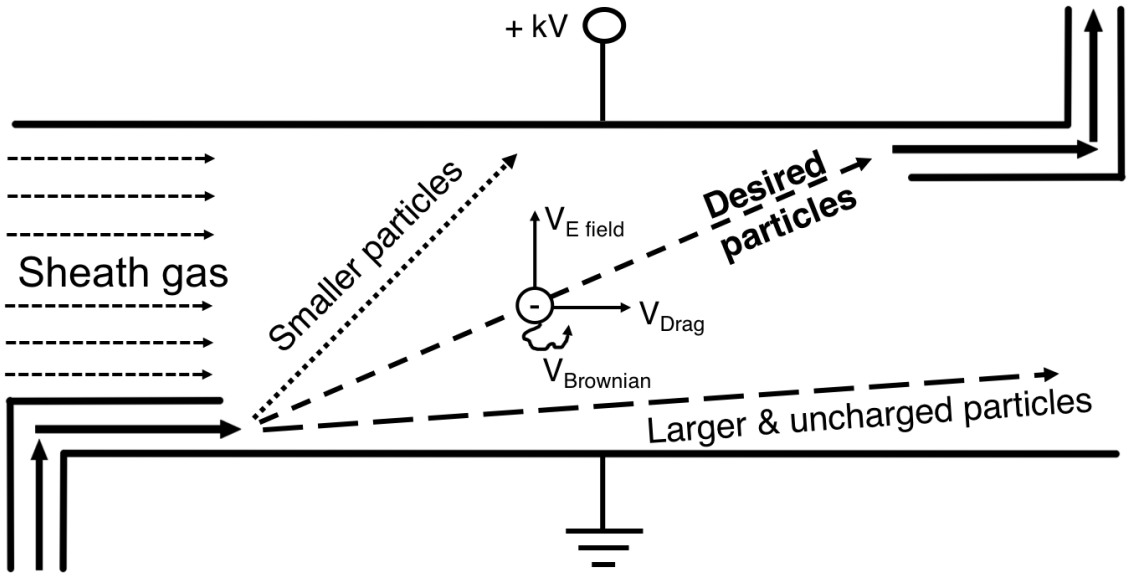

Figure 2.2: A diagram of the operation of a differential mobility analyser to select particles based on their electrical mobility diameter Z. Figure inspired by [16].

2.3 Nanoparticle Deposition

For large particles this would seem not to be a problem, place a surface in the gas flow and direct particles onto the surface to deposit them. However, for nanoparticles this is not possible. Nanoparticles have very low inertia and will change their motion to adjust to the direction of the gas flow. This means that the vast majority of nanoparticles will not be deposited onto a surface and instead follow the direction of the gas flow around the surface. To solve this problem an external electric field is applied to deposit the particles in the aerosol system.

In order to analyse nanoparticles outside of the aerosol system and use other characterisation techniques the particles are deposited onto a substrate using an electrostatic precipitator (ESP). An ESP works similarly to a DMA but instead of sorting by electrical mobility it uses an applied electrical field parallel to the direction of the particles. This collects all the charged particles from the system regardless of size. An electrometer is connected in the aerosol system for an online measurement of the particles, it measures the current and because most of the particles are singly charged this gives a good estimate of concentration of the particles. This is important because a particle flow rate of at least 10^6 particles per second is necessary to provide sufficient substrate coverage for a good analysis of the nanoparticles [16]. Once the particles are deposited onto a substrate the particles stay on the surface due to van der Waals forces, gravitational and inertial forces are negligible for nanoparticles so the particles do not move unless contacted directly.

2.4 Magnetic Nanoparticles

Magnetism is an interesting phenomenon that has always had a mysterious nature because it is a seemingly invisible force that can work over large distances. However, in reality magnetism is one of the most important forces for techniques and applications in the everyday world. Magnetic nanoparticles are nanoparticles which are made from elements such as cobalt, iron, nickel, manganese as well as other ferrite materials. If magnetic nanoparticles are sufficiently small in the range of 1 - 100 nm, then their magnetisation can change direction under the influence of temperature. In the absence of a magnetic field the particles switch fast enough that the magnetisation is a net zero and the nanoparticles are in a superparamagnetic state. The magnetic nanoparticles have a much higher magnetic susceptibility than normal paramagnetic materials meaning that the nanoparticles can be magnetized by an external field to a high degree. The magnetic nanoparticles are small so enable targeted therapy but also have a high degree of controllablility. These properties allow magnetic nanoparticles to have enormous potential for drug delivery in medical applications [17]. Magnetic nanoparticles can act as a carrier of a drug which is attached to the particle and inject intravenously, a magnetic field is applied which retains the particles in the targeted region [18].

A second property that gives magnetic nanoparticles significant potential is the magnetocaloric effect. When exposed to a magnetic field the temperature of a magnetic material increases and cools down when the field is removed. This in combination with nanoparticles large surface area to volume ratio enables a greater amount of heat to be transferred to the environment [19]. These properties are motivating research into experimental cancer treatments that target the tumour with magnetic nanoparticles. Magnetic nanoparticles can be inserted into a tumour and if a patient is subjected to an alternating magnetic field then the tumour heats up potentially enhancing the oxygenation and chemosensitivity of the tumour by a process called magnetic hypothermia [20]. The novel properties of magnetic nanoparticles are driving research into other applications outside of medicine such as in the protection of the environment via the treatment of contaminated water [21] and as catalytic supports for transferred hydrogenation [22]. Samarium-cobalt is a candidate material that has already shown the potential to create nanometer structures that display magnetic properties [23]. However further investigation is needed into this material's production in order to understand if samarium-cobalt nanoparticles are viable magnetic nanoparticles.

2.4.1 Samarium-cobalt magnets

Samarium-cobalt magnets are a popular type of rare earth magnet, which in bulk acts as a strong permanent magnet. Magnets can be used to create different types of motions which can be harnessed in a plethora of applications. The motion of an electric current against a magnetic field in a motor can convert electric energy into mechanical energy and is used in almost all electric cars. Samarium-cobalt magnets have a high coercivity which means they are highly resistant to demagnetisation by external magnetic fields making them good candidates for motor generators. The two most common elemental compositions are $SmCo_5$ and Sm_2Co_{17} for SmCo magnets which are both rich in cobalt [24]. Samarium-cobalt magnets are the second most popular magnet after neodymium magnets which are more powerful magnets. However, SmCo magnets are the superior option if

the magnet needs to operate in more challenging environments because they have a high magnetic power over a large range of temperatures. SmCo magnets are more expensive than neodymium magnets but their unique properties make them a potential candidate material for nanoparticles that have magnetic properties.

Magnetism is a phenomenon that occurs when electric charges move in the presence of a magnetic field. Rare earth magnets are the strongest type of permanent magnet that can be made today. Permanent magnets are made from ferromagnetic materials which produce a constant magnetic field which differ from electromagnets because they cannot be turned off. The different ways in which materials react in a magnetic field allows them to be grouped into four categories. There are four classes of magnetic behaviour: diamagnetism, paramagnetism, ferromagnetism and ferrimagnetism which are closely related. Samarium-cobalt magnets are ferromagnetic so a basic description of ferromagnetism will be presented.

2.4.2 Ferromagnetism

The atoms in the lattice of ferromagnetic materials are arranged in such that atomic magnetic moments align parallel to each atom. These magnetic domains decide how the material will react in the presence of an external field. Magnetic domains are small magnetized regions in the material which are randomly oriented, the random orientation usually means that the domains cancel out leaving the overall material unmagnetized. An external field can be applied which if large enough causes the magnetic domains to re-position themselves to align with the direction of the magnetic field, giving a net magnetisation. How the magnetic domains in a ferromagnetic material such as samarium-cobalt behave both in the presence and absence of a magnetic field is illustrated in Figure 2.3. Only the materials Fe, Co and Ni are ferromagnetic at room temperature, however above a material-specific temperature the thermal agitation is large enough that the material loses its ferromagnetic nature which for samarium cobalt magnets is temperatures above 350^{o}C.

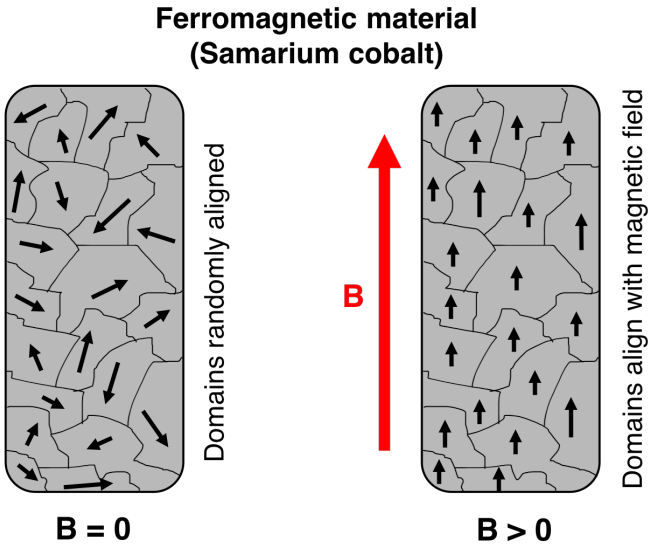

Figure 2.3: Illustration of the ferromagnetic material such as samarium cobalt before and after being exposed to an external magnetic field.

Chapter 3

Electrodes, NP Synthesis and Analysis

The first part of the project is to investigate if pure samarium-cobalt electrodes can be successfully produced. The electrodes were fabricated using two devices and pressed using the equipment at the department of mechanical engineering at LTH. The second part of the project is to produce SmCo nanoparticles from three different source materials. The synthesis of nanoparticles can be made in many ways including mechanical methods, vacuum methods, chemical methods and aerosol methods. Aerosol methods have advantages in their flexibility by giving a user good control over the production of the particles when compared to other methods. Creating nanoparticles from SmCo is not a well understood process so using a more versatile production method can give freedom when trying to understand the best way to synthesise the particles. Spark discharge generation ablates material on the atomic level which enables very good mixing of elements into alloys [25]. For these reasons Spark discharge generator (SDG) is the aerosol method chosen for this work. An SDG uses two metallic rods which are the materials from which the nanoparticles are produced. SmCo nanoparticles were hoped to be formed by creating electrodes from mixed samarium and cobalt powder. The final part of the project was to analyse the different SmCo nanoparticles from the different source materials using characterisation tools and techniques.

In this chapter I will present how electrodes were produced from raw materials and how these electrodes can be used in a spark discharge generator to create nanoparticles. I will explain in stages how the electrodes were sintered and how a spark discharge generator can be used to generate nanoparticles. I will end the chapter by presenting some of the analysis techniques that can be used to characterise the nanoparticles that are synthesised.

3.1 Pressing Electrodes

Electrodes are usually made by pressing raw powder under force and then sintering at high temperatures to cause the material to coalesce into a solid mass. In this project samarium-cobalt electrodes will be attempted to be produced by pressing a mixture of samarium and cobalt powders with force and without additional heating. SmCo is a material commonly used in permanent magnets which were first produced in the 1970s. The manufacturing process to create samarium-cobalt magnets contains a few steps. Trace impurities of iron, copper, hafnium and zirconium are added to improve the heat treatment

process and produce a better alloy. The raw elements are heated together in an induction furnace filled with argon gas and melted to form the SmCo alloy which is then grounded down to particles. The particle powder is pressed into a die and heated up to temperatures of 1250^{o}C, this fuses the particles into a solid alloy [26]. The samarium-cobalt is then cooled in the presence of an electric field, coated and then magnetized. SmCo is a material which is magnetically anisotropic which means that it can only be magnetized in the same axis as the magnetic orientation. Pure SmCo electrodes cannot be purchased and neither can other electrodes with a tailored elemental composition. The motivation behind the first part of the project is to investigate if electrodes can be successfully produced from mixtures of different elements.

The mixing and pressing of samarium and cobalt micro powders into electrodes is not common so first the procedure to press the particles was practised using stainless steel (SS) powder. Samarium powder can be dangerous as it spontaneously combusts at temperatures above 150^oC so it must be handled carefully. Cobalt is also dangerous to human health at high concentrations. If high concentrations of cobalt enter through the lungs, then people can experience effects such as asthma and pneumonia. To avoid excessive exposure to these potentially dangerous elements the pressing method was practised by first pressing electrodes using safe stainless steel grade 430 powder.

In this project the tools were not available to replicate a multi-step sintering process with complicated heat treatment and machining. Instead samarium-cobalt electrodes were attempted to be produced by pressing a mixture of the samarium and cobalt micro powder only with force, without additional heating and without the addition of impurities. The SmCo electrodes were pressed by mixing the rare earth metal powder and cobalt together in the ratio of $SmCo_5$. The powders were weighed out individually to fulfil the ratio of $SmCo_5$ and then both poured into a container. The container was placed in a device called a mixer for 5 minutes which rotates the container blending the powders together to give a consistent and homogeneous mixture of the samarium and cobalt powders. The mixture of powders was then poured into the chamber of the pressing tool. Two pressing tools were used throughout the project, the first tool consists of a steel cylinder with a central chamber to pour in the powder, a removable base and a plunger which is in contact with the hydraulic press piston. A picture of the first cylinder-shaped tool can be seen in Chapter 4 Figure 4.1. The second tool consists of two blocks that interlock together to form the device with a central chamber to put the mixture of powder into. The block tool was designed to separate into two parts allowing the electrodes to be removed more easily after pressing. A second improvement was that the plunger dimension were changed to improve the solidity of the plunger under the force of the hydraulic press. A photograph of the second block tool is shown below in Figure 3.1.

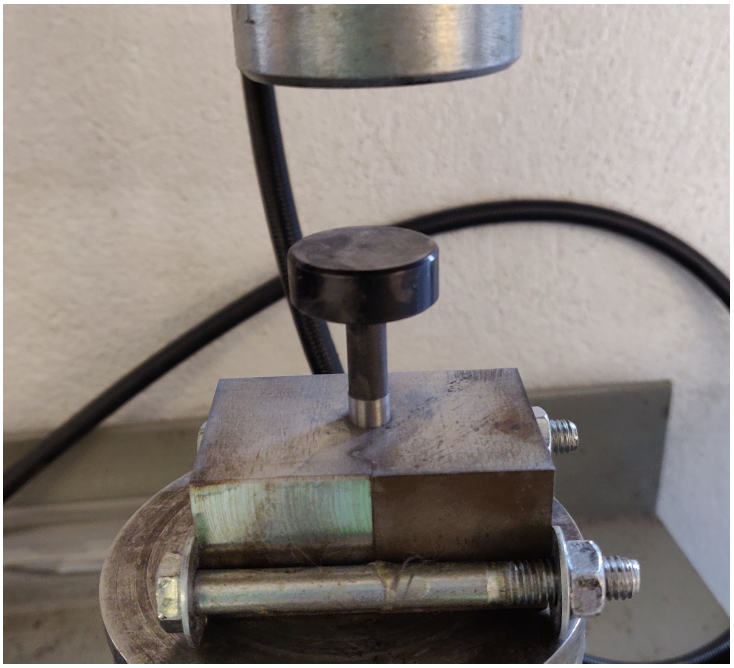

Figure 3.1: Image of the second tool before being pressed by the hydraulic press.

After discussion with the project supervisor about the experiences with attempting to sinter the stainless steel powder it was decided not to continue with the pressing of the samarium-cobalt powder. This was due to the degree of difficulty in attempting to sinter with both devices and because of the increased dangers of attempting to sinter with samarium and cobalt powder without a successful device and a clear method. The project moved onto the second part which was the fabrication of magnetic nanoparticles in the SDG from the two production materials. The first production material is two identical alloyed samarium-cobalt containing impurities, the second material is two different electrodes one of pure samarium and the other of pure cobalt. The objective is to see if it is possible to fabricate SmCo nanoparticles that have the same composition as many permanent magnets and so potentially the same magnetic properties.

3.2 Spark Discharge Generator (SDG)

The spark discharge generator is made up of a number of different components that fit together in a telephone box sized rack of length 0.5 m, width 0.5 m and height of 2 m. A photograph of the entire spark discharge generator setup including the electronic controls (bottom left) and external furnace control (middle left) is shown in Figure 3.2. The two main systems of the spark discharge that are needed to generate nanoparticles are a chamber to house the metallic electrodes with a gas flow to remove material and an electric circuit to induce the generation of a spark between the electrodes.

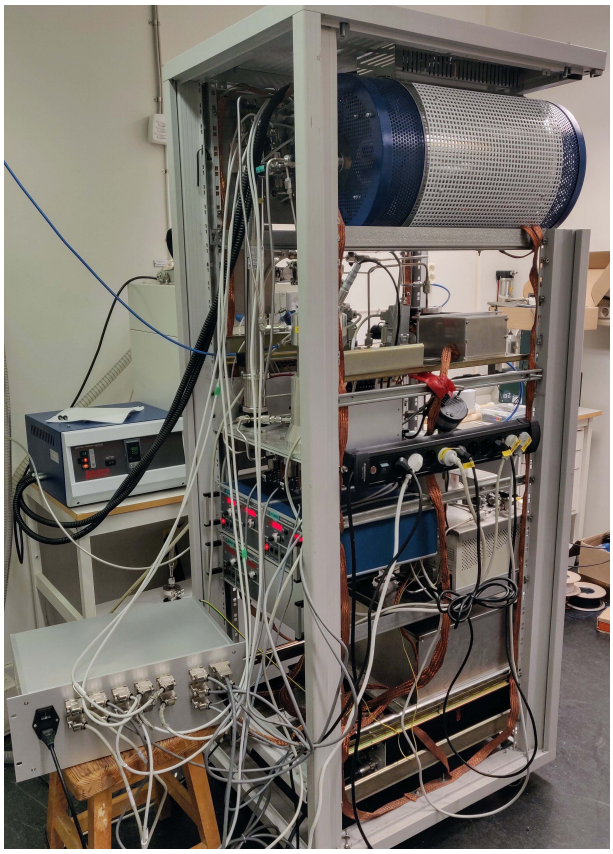

Figure 3.2: Photograph of the entire spark discharge generator setup

3.2.1 SDG layout

A spark discharge generator consists of many different parts that in combination form the machine that can generate nanoparticles. The generation of the particles begins in the chamber which houses the two electrodes, these two metallic, conducting rods are placed so that they face each other. The electrode positioned on the left is charged and acts as an anode inducing a high voltage across the electrode gap to the electrode on the right which acts as the cathode. Eventually when a high enough voltage is attained a spark is induced across the gap between the two electrodes positioned to the right electrode which is grounded, the spark then oscillates between the two rods enabling material from both rods to be ablated. The material at the end of the rod where the spark is induced is ablated and if rods of two different compositions are used then an alloy of the two elements is produced. The carrier gas transports the cloud of particles away from the spark, a small overpressure in the system keeps the flow of the carrier gas constant enabling consistent production. The cloud of particles is made up of smaller primary particles and agglomerates. The system operates at a near ambient pressure of 1015 mbar and is pumped down to 15 mbar to purge any other gases such as oxygen from the system before nanoparticles are generated. Oxygen in the system can lead to oxidation of the nanoparticles changing their behaviour in undesired ways, this will be discussed further in Section 3.2.6. Figure 3.3 shows the setup of the spark discharge generator used in this work and shows how the particles are directed into the different parts of the machine.

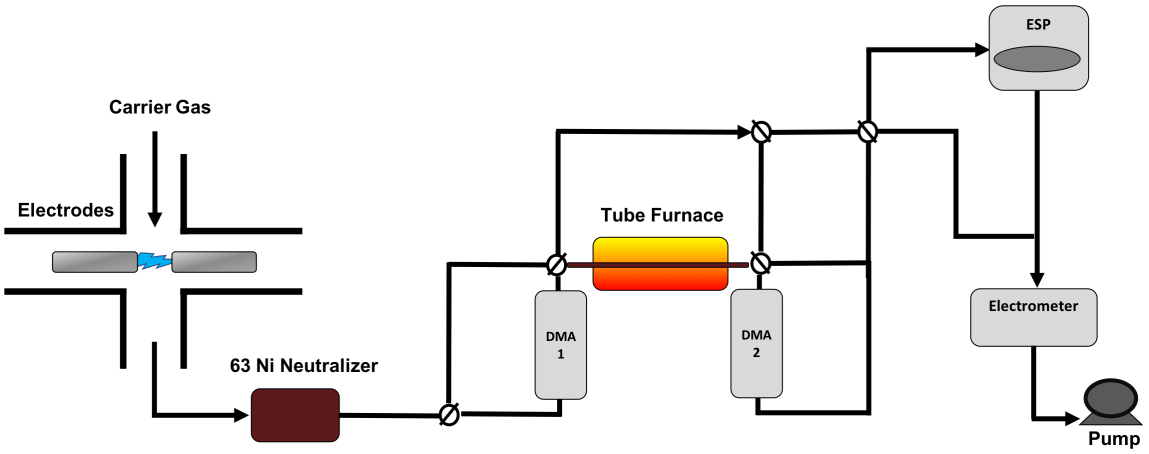

Figure 3.3: Schematic image of the spark discharge generator setup. Showing how particles are generated and move through the system. Image inspired from "Generation and Deposition of Magnetic Aerosol Nanoparticles" By Calle Preger [14].

It can be seen in equation 2.5 that the particles must be singly charged to differentiate between their mobility diameters. Multiply charged particles of the same geometric diameter will have a decreased electrical mobility diameter so it is essential to ensure particles of the same charge are produced. To create a known charge distribution the agglomerate particles are swept away by the carrier gas and into a ^{63}Ni neutraliser. A pair of differential mobility analysers (DMA) work in tandem to allow particles to be sized selected before and after a tube furnace which heats up the agglomerates allowing how they compact into different shapes to be studied. How the shape of particles compacts and change at higher temperatures will be discussed further in Section 3.2.4. The output particles can then be directed towards an electrostatic precipitator (ESP) which applied an accelerating voltage allowing the particles to be deposited and removed for further analysis, this will be discussed in Section 3.4. The final part of the SDG setup is an electrometer which gives an in situ measurement of the concentration of the particles at the point of deposition in the ESP.

3.2.2 Spark ablation

In the SDG chamber the two cylindrical electrodes are separated by a gap which can be changed but is maintained during ablation. A series of capacitors is connected to the left electrode which is charged by a high voltage power supply. When a breakdown voltage of 2 kV is reached the capacitors discharge instantly creating a spark across the gap between the electrodes [27]. Two important parameters can be changed to optimise the production of particles for specific types of electrodes. Firstly, the current C which is related to the frequency of the spark f by equation 3.1 where I is the charging current of the capacitors and V_b is the breakdown voltage.

$$f = \frac{I}{CV_b} \tag{3.1}$$

Increasing the frequency of the spark results in an increase in the concentration of the number of particles and also shifts the distribution of particles to larger sizes [28]. Secondly the carrier gas flow which moves the particles away from the spark and into the rest of the machine. The sparks impact on the second electrode positioned on the right creating an extremely high local temperature resulting in the ablation of the electrode

material on both electrodes. Primary particles are formed by homogeneous nucleation due to the cloud of metallic vapour being supersaturated. The metallic vapour begins to cool as the carrier gas transports the vapour away and begins to coalesce into larger particles. The primary particles coalesce because at this stage in the growth the collisions have enough energy to form complete particles. There is a further stage of growth of particles when the primary particles condense and coagulate. The final result is a high concentration of charged, agglomerate nanoparticles. The particles will maintain their size since there is no additional vapour and no coagulation [16]. These two stages are the two growth stages of nanoparticle production and at this point the concentration is at a maximum.

Spark discharge generation enables great mixing because the nucleation is on an atomic level and the material cools rapidly meaning that metallic alloys can be formed more easily [29]. The dual electrode setup used in the SDG chamber enables the formation of bimetallic particles from the two electrodes which can be made of different elements or from alloyed material. The composition of the nanoparticles depends on the electrode material but also the electrodes position. The left electrode acts as the positive anode and the right electrode acts as the negative cathode. The cathode electrode is always ablated more strongly and thus contributes more material to particles than the opposing anode electrode [30]. There is evidence that one of the contributing factors to this phenomenon is the collision of charge carriers with the cathode electrode. Positive ions that have greater energy are attracted to the cathode which causes stronger ablation than on the anode [31]. A photograph of the spark ablating material from a pair of electrodes in the SDG setup can be seen in Figure 3.4 below.

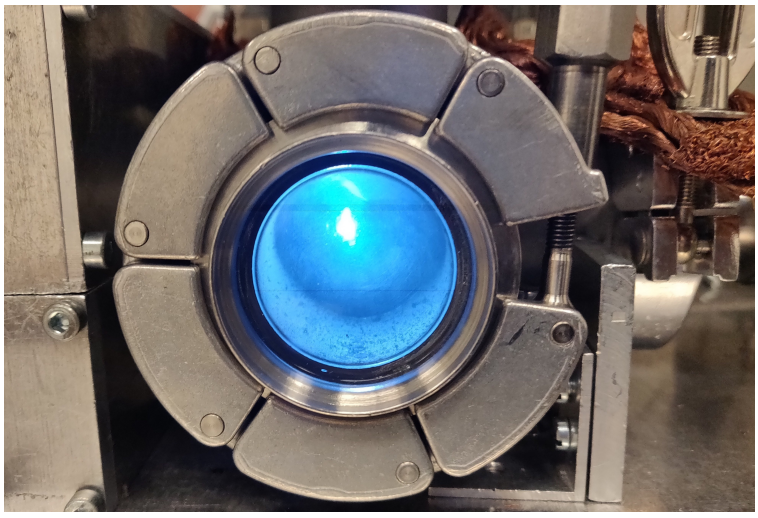

Figure 3.4: Image of the spark ablating material from electrodes in the SDG chamber.

3.2.3 Compaction of agglomerates

After the spark discharge the vaporised metallic electrode material begins to form agglomerate particles. These agglomerates have open, string-like structures which are not the compact, spherical shapes which are ideal for most nanoparticle applications. Therefore the agglomerate particles are compacted in order to create ordered, uniform nanoparticles. As the particles are heated at a material-specific temperature, they begin to compact by reshaping their morphology into more spherical shapes. The compaction is performed

by heating the agglomerate particles. The reshaping of the agglomerates causes a morphological change which causes a decrease in the particle's electrical mobility due to a more streamlined shape. The particles are analysed in the differential mobility analyser (DMA) which detects smaller particles after the compaction particles, but importantly the particles contain the same mass as the agglomerates. The compaction temperature is defined loosely as the temperature at which no significant decreases in mobility diameter occur. The compaction temperature T_c of the samarium-cobalt agglomerates is measured by observing how the size distribution of particles changes at various temperatures. The compaction temperature depends on the initial electrical mobility diameter of the agglomerates but is also material dependent and is closely related to the materials melting temperature T_m. For metallic materials T_c should be between 1/3 and 1/2 of T_m and for particles that are oxidised the temperature is larger, closer to 2/3 of T_m [32].

3.2.4 Thermal charging

The spark discharge generates ionised particles that can display a number of charges. The agglomerate particles carry random numbers of charges so a ^{63}Ni neutraliser is used in the aerosol system. However, unlike the name suggests this device does not neutralise the particles instead it gives the particles a known charge distribution. This distribution is the Boltzmann equilibrium charge distribution which gives most of the particles neutral charge, a small fraction a single positive or single negative charge and a very small number will have multiple charges [7]. At high temperatures an unexpected phenomenon occurs, the particles begin to be charged thermally by the furnace. This often occurs in the range of 900^{o}C to 1100^{o}C and at higher temperatures the thermal charging decreases and eventually disappears. The number of charges of the ions and for which temperatures they appear varies with the type of carrier gas and the composition of the nanoparticles. The multiply charged particles are a problem since the particles are detected at lower mobility due to the charge dependence of the electrical mobility as shown in equation 2.5. This reduces the relative intensity of the dominant single negatively charged peak in the size distribution. The -1 peak is used to analyse the particles by comparing how their mobility changes against temperature. Thermal charging makes the identification of the -1 peak more difficult since a convolution of the peaks is often observed over a wide range of mobility diameters. Examples of thermal charging can be seen in Chapter 5 Figures 5.5 and 5.13. Thermal charging behaviour has been identified in other materials, but a satisfactory explanation has not been determined [33].

3.2.5 Particle oxidation

The spark discharge generator is under ambient conditions and despite pumping the system down and purging the system of air it is difficult to completely remove oxygen. When the particles are produced in the SDG some of the remaining oxygen molecules in the chamber oxidise a considerable fraction of the nanoparticles. A method to try to prevent the oxidation of particles is to use a carrier gas that has a fraction of hydrogen which reduces the number of oxidised particles.

All non-precious metals oxidise, in the presence of oxygen the surface of metals corrode to form a layer of the metal oxide on the surface. This process also occurs for nanoparticles and is governed by the *Cabrere-Mott* model. Oxidation is driven by a particles electric

field, a non-oxidised particle's surface is exposed to oxygen can easily react with the surface to form an oxide layer. As the oxide layer increases a larger electric field is needed to penetrate the layer and oxidise the non-oxidised parts of the metallic particle. The layer at which the oxidisation stops is called self-passivation Samarium oxides relatively slowly to form a layer of Sm_2O_3. In this thesis two carrier gases of pure nitrogen and nitrogen with 5% hydrogen were used to investigate how samarium-cobalt nanoparticles oxidise.

3.3 Nanoparticle Analysis Instruments

The important tools and techniques used to analyse the samarium-cobalt nanoparticles that were produced from different sources.

3.3.1 Scanning Electron Microscope (SEM)

A visible light microscope is limited to a magnification of around 1000, this means that objects below 200 nm cannot be resolved. This is because diffraction sets a limit on the resolving power using white light in the visible spectrum of 400 - 700 nm. Electrons can have much smaller wavelengths which are based on their energy or accelerating voltage when used in a scanning electron microscope (SEM). An SEM uses a high energy focused beam of electrons to scan over a surface, the electrons interact with the sample and produce a signal via secondary electrons, backscattered electrons and characteristic x-rays. These signals are assembled to create an image of the sample giving topographical information as well as compositional [34].

A scanning electron microscopy (SEM) was used in this work to determine the approximate size and shape and coverage of the particles after being deposited onto a silicon substrate. An SEM is quite a sensitive tool which makes it possible to differentiate between different nanometer-sized particles to understand how they change under different conditions such as carrier gas and temperature.

3.3.2 TEM and EDX

A Transmission electron microscope (TEM) is one of the best ways to study nanoparticles because of the high-resolution capabilities which can give atomic resolution. The morphology of particles can be studied in detail. In combination with TEM, Energy dispersive X-ray spectroscopy (EDX) was performed using an additional instrument attached to the TEM. This tool measures the photon energies of characteristic X-rays emitted from the sample when exposed to high energy radiation. This is a good characterisation technique because it allows the elemental composition of nanoparticles to be determined to help to understand how they are produced.

Chapter 4

Pressed Samarium-Cobalt Electrodes

In this chapter the results of attempting to press samarium and cobalt powder into samarium-cobalt electrodes will be presented. The results of pressing the stainless steel electrodes produced in order to practise the pressing method are displayed. These results will be discussed in the context of the material presented in the previous chapters. The results of the different presses will be discussed to evaluate the viability of pressing custom electrodes from a mixture of powders.

4.1 Cylinder Pressing Tool

The stainless steel powder was weighed out in the ratio of samarium-cobalt $SmCo_5$ to practise the weighing and handling of micro powders. The powders were placed in a single container and put in the mixer at a frequency of 45 revolutions per minute. The mixed powder was then added to the first cylinder tool. The dimensions of the chamber and thus the plunger which is pushed into the chamber have a length of 80 mm and diameter of 8 mm, a photograph of the first cylinder tool can be seen in Figure 4.1. The cylinder sintering tool was placed under a hydraulic press and an estimation for the amount of force was made based on the yield strength of the material to give some baseline for the amount of force that would be required. Several reliable sources list the yield strength of stainless steel 430 as 2.05×10^8 N per m^2 [35], the yield strength is the amount of force required to cause the material to deform permanently. The tensile strength is listed as 4.50×10^8 N per m^2 [35] this is the ultimate amount of force a material can withstand without rupturing. The area of the top of the electrode in contact with the press is multiplied with the mechanical properties and compared to the amount of force generated by the hydraulics press pistons which is given in terms of pressure. This gave a range of pressures using the first tool of *53 to 115 bars* of pressure. The hydraulic press can produce a pressure of up to 1000 bars which is equivalent to about 20 tons of force on the powdered material.

Figure 4.1: Photograph of the first electrode sintering tool.

4.1.1 Stainless steel electrodes

Based on the estimations to deform the material the powder was pressed at increasing pressures of 60, 80, 100 and 110 bars of pressure. At 60 bars of pressure the electrodes produced were very weak, large pieces of the electrodes began to break off almost immediately. The electrode was handled carefully and attempted to be stored in a container, but it began to collapse and only chunks of powder remained after being placed in the container. Due to this result it was decided to increase the pressure of the hydraulic press to 80 bars. This produced a sturdier electrode which can be seen in Figure 4.2 (a). The electrode pressed at 80 bars was sturdier when compared to the electrode produced at 60 bars, however the electrode was still quite porous with parts at the top easily breaking away. This gave the top of the electrode an uneven surface, loose material on there is not ideal since the top of the electrode is where the material is ablated in the SDG. There were concerns about the overall solidity of the electrode as the top surface needs to be able to withstand the energy of the spark and the sides need to be held tightly in position in the SDG chamber. The pressure was increased again to 100 bars to try to produce an even sturdier electrode the result of which can be seen in Figure 4.2 (b).

(a) 80 bars

(b) 100 bars

Figure 4.2: Pictures of the pressed stainless steel 430 electrodes using the first cylinder tool at pressures of (a) 80 bar and (b) 100 bar.

The 100 bar electrode was even sturdier with only a very small amount of erosion at the edges and overall the rod felt much more solid when placed into storage compared to the 80 bar electrode. Comparing the two electrodes shows the increased evenness of the top of the electrode and the more silver, steel-like colour of the 100 bar electrode demonstrating its increased strength. The electrodes at 100 bar were deemed sturdy enough to be tested in the SDG so two more electrodes were produced to test in the SDG. The 100 bar electrodes were deemed successful, but the pressure was increased again to 110 bar to see if even more solid electrodes could be produced. Unfortunately, at a higher pressure of 110 bar the force on the plunger of the tool became too large and it began to deform causing the plunger to bend and impact upon the chamber. This made the device inoperable since the plunger could no longer be inserted into the chamber and no more electrodes were able to be produced with the first tool. A second electrode pressing tool was manufactured with improved specifications to counteract the flaws that had become apparent with the first device.

4.1.2 Spark tested electrodces

The 100 bar electrodes that were successfully pressed were used in the spark discharge generator to see if they could withstand the energy of the spark impacting on the electrodes surface. The spark discharge generator was run for 2 hours at a discharge voltage of 3 kV and driver currents of 5 and 10 mA, these are typical settings for other electrode materials. A photograph of the electrodes after being used to generate particles in the SDG can be seen in Figure 4.3. The electrodes withstood the energy of the force well, erosion occurred at the charred ends of the electrodes but that is expected as this is where the spark impacts on the electrode. There was no further erosion on the sides of the electrodes where it is gripped in place in the SDG chamber or at the other end of the electrode. The result of testing these electrodes is a positive indication that pressed electrodes can be made and used in the spark discharge generator successfully.

Figure 4.3: Photograph of two stainless steel electrodes pressed at 100 bars after being used in the SDG with the end exposed to the spark discharge facing up. Note the light silver colour on the top of the electrode indicating where the spark ablates material from the electrode.

Overall the results of the pressing of the stainless steel powder are positive. The electrodes were pressed at pressures in the range where the stainless steel powder was expected to begin to coalesce into a solid rod. The indications for producing samarium-cobalt

electrodes are good since steel is often produced by sintering at high temperatures in a similar process as SmCo [36]. Nonetheless in this work it has been shown that it is possible to produce electrodes pressed only with force that are compatible with plasma-based spark discharge generation. If the tool is improved by strengthening the plunger and perhaps widening the electrode dimensions to create electrodes with larger diameters, I believe that samarium-cobalt electrodes can be produced.

4.2 Block Pressing Tool

A second device was manufactured which consists of two blocks that have interlocking notches which allow the blocks to lock together to form a central chamber which holds the powder. The two blocks were clamped together with an external clamp to keep them together when being pressed. The block tool was designed to allow the electrodes to be removed more easily after being pressed. A second improvement was that the plunger dimension was changed by decreasing the length to 50 mm and increasing the diameter to 10 mm. These changes were made to make the plunger stronger than the first tool and make it more resistive to the force from the hydraulic press. stainless steel 430 powder was used again to practice pressing using the new second tool. A similar estimation as for the first tool was made to give a range of pressures that would be a guide for the pressures to press the electrodes with. The increased size of the chamber of the block tool allowed for a greater amount of force and thus pressure to press the electrodes with. The range of pressures for the second device was *82 to 180 bars*.

4.2.1 stainless steel electrodes

The larger electrodes mean that more pressure needs to be applied to provide the same level of compression as the smaller electrodes. Based on the pressure estimate the rods were pressed at pressures of 80, 100 and 120 bars. At pressures of 80, 100 and 120 bars when the clamp was removed the electrode material became stuck to the chamber with one half attached to one half of the block tool and the other half to the opposite block. The material was stuck to the device's chamber and was very laborious to remove, a photograph of this can be seen in Figure 4.4. To prevent this from occurring a number of solutions were proposed. Firstly, a stronger clamp was used to stop the two blocks from potentially moving during the press, causing the electrode to split in half before being fully fused. Unfortunately, this appeared to have no effect as the result was the same, when pressed at 100 bars after the clamp was removed the two halves of the electrode were stuck to the chamber. A second proposed solution was to lubricate the sides of the chamber with the multipurpose lubricant WD-40 to try to stop the powder from becoming stuck when pressed. Again, this failed, when pressed at 100 bars the same result occurred with two halves of the electrode stuck to the chamber. A final attempt to produce electrodes was made, after the press the two blocks were kept clamped together and the tool was positioned so that the electrodes could be pushed out through the chamber. Very high pressures of up to 200 bars were applied with the press to try to push the electrodes through the chamber however the electrodes remained stuck. Higher pressures were not attempted as the 200 bars is already larger than the pressures applied to initially press the electrodes. This made the final attempt feel uncomfortable as larger force should not be required to remove electrodes then were used to produce them. Samarium and cobalt powders are more dangerous than steel so if any part of the steel pressing procedure felt

unsafe than it would be much more dangerous using samarium and cobalt powders.
Sadly, no stainless steel electrodes were successfully produced using the second block tool. The powder became stuck to the sides even at the same pressure of 100 bars as used for the first tool, this may be down to the separable block design of the tool. Even when subjected to high pressures of 200 bars the powder remained stuck this would suggest that there is some fusing occurring with the powder and the tools chamber. The two block design was a flawed design which allowed the electrodes to crack in half and required a large, unwieldy external clamp during the pressing. The first tools cylinder design was a better design overall, but the dimensions of the plunger were inadequate because it was too long and had too small a diameter meaning it was deformed by the hydraulic press.

Figure 4.4: Two halves of a stainless steel electrode pressed at 100 bars stuck in the chamber of the second block tool.

Chapter 5

Samarium-Cobalt Nanoparticle Analysis

The final part of the project was the analysis of the samarium-cobalt nanoparticles produced from the different electrodes in the spark discharge generator. The first type of electrode material was alloyed SmCo electrodes that were previously permanent magnets. The magnets were placed in a furnace and heated to 800^oC, a temperature above the Curie point for SmCo thus demagnetising the magnets. The second type of electrode material was an electrode of pure samarium and another of pure cobalt. This chapter will investigate each production source of the SmCo nanoparticles by examining the particles through the driver current, furnace temperature and by using SEM and TEM instruments. The results of each production source will be discussed in the context of aerosol theory and also with similar research performed on other types of nanoparticles. The production sources of the SmCo will be compared to determine the differences in the output particles and discover which source is more suited to nanoparticle generation.

5.1 Alloyed Samarium-cobalt electrodes

To configure the production of SmCo nanoparticles from the alloyed electrodes the parameters of electrode gap and driver voltage need to be set. The first DMA was scanned across a wide range of mobility diameters to give the particles size distribution and the peak concentration at gap distances of 1, 2 and 3 mm. A gap distance of 2 mm between the electrodes was chosen as it produced particles that were smoothly distributed at high concentrations with no sudden peaks in concentration at particular mobilities. The 2 mm gap was maintained for all of the measurements using the SmCo electrodes. The driver voltage must be set firmly above the breakdown voltage of the spark in the SDG. A typical value of 10 kV was set and the breakdown voltage with the alloyed SmCo electrodes was in the range of 2 - 4 kV so a value of 10 kV was maintained.

5.1.1 Driver current

Increasing the driver current increases the frequency of the spark shown in equation 3.1, a higher spark frequency increases the concentration of the particles and also shifts the distribution to larger particle sizes. Changing the driver current allows nanoparticles of a desired size with a sufficient concentration to be produced.

To investigate which sizes of SmCo particles can be produced with sufficient concentration the driver current was set from 5 to 30 mA in intervals of 5 mA. Examining the driver currents also helps to find the current that gives a smooth size distribution that peaks at a sufficiently high concentration for accurate analysis and depositions. Scanning the first DMA at room temperature gives the size distribution of the agglomerate particles but not the size distribution of the compacted particles. The second set of driver current measurements are made at a temperature of 1000 degrees at which the particles are expected to be compacted based on the melting temperature of SmCo. Figure 5.1 (a) and (b) shows the results of varying the driver current on the size distribution of the particles at RT and 1000^{o}C.

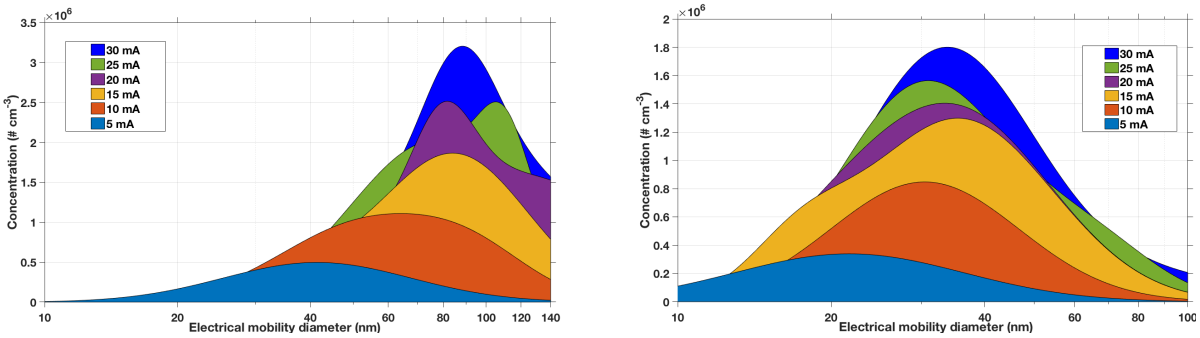

(a) RT **(b)** 1000^{o}C

Figure 5.1: The size distribution of particles produced from alloyed SmCo electrodes as the driver current is increased at temperatures of (a) RT and (b) 1000^{o}C.

Figure 5.1 (a) the observed increase in the number concentration of the particles and shift in the size distribution to higher mobilities is in agreement with other electrode materials [30][37]. Figure 5.1 (b) shows that as the driver current is increased from 5 - 15 mA the concentration rises rapidly but begins to plateau with only a small difference between doubling the current from 15 to 30 mA. This behaviour is expected and has been observed in other materials [30]. This behaviour and the widening of the size distribution can be explained by more coagulation occurring at higher concentrations. At a large current and spark frequency the primary particles cannot be removed by the carrier gas fast enough to allow the spark to ablate more material from the electrodes. Consequently, further increases in the current lead to an increase in the mobility diameter and not the number of particles. Figure 5.1 (b) shows that to obtain a relatively large number concentration of 40 nm particles a higher driver current above 10 mA is needed. Conversely to obtain small nanoparticles of 10 nm or smaller the optimum driver current is below 5 mA. For the analysis of the particles no particular size is desired so a driver current of 15 mA with a balanced size distribution was selected. Figure 5.1 (a) shows that for 15 mA the peak of the size distribution occurs at 80 nm hence the first DMA should be set at 80 nm to let in the highest concentration of agglomerate particles. (b) shows that the compacted particles using 15 mA will be at high concentrations in the range of 20 - 50 nm.

5.1.2 Compaction

The primary particles produced from the spark ablation collide to form agglomerate particles which have open, irregular structures. These agglomerate particles are not spherical in shape and their unpredictable morphology makes them more difficult to analyse and

unsuitable for most nanoparticle applications. To improve the particles suitability the agglomerate particles are compacted by increasing their temperature using a tube furnace.

To investigate the temperature at which the SmCo particles compact second DMA after the furnace is scanned across a range of temperatures. The dominant -1 peak is used to compare how the mobility diameter changes with temperature. A plot of these mobilities against temperature is called a compaction curve and shows how the morphology of agglomerate particles changes with temperature. The compaction curve is measured using both carrier gases of pure nitrogen and 5% hydrogen. The different carrier gases investigate the differences in compaction under different gas conditions. Figure 5.2 shows the compaction curve for both carrier gases.

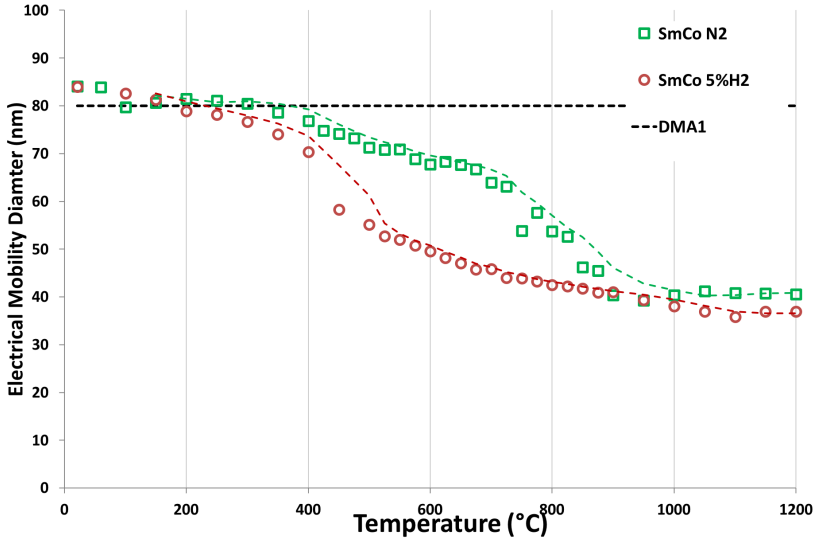

Figure 5.2: Compaction curve of SmCo nanoparticles with mobility diameter against temperature using nitrogen and 5% hydrogen. Dashed lines show a 3 point moving average trendline.

In Figure 5.2 SmCo particles generated in pure nitrogen compact gradually over the temperature range before reaching a final diameter around 40 nm above the compaction temperature of 900^{o}C. In contrast, particles generated with a 5% hydrogen compact at a lower temperature of approximately 700^{o}C and reach a lower mobility diameter of around 36 nm. The observed shapes of the nitrogen and 5% hydrogen mixture curves are expected and in line with the findings of other materials such as Co, Sn [38], Au [39] and Fe [14]. Moreover, the compaction temperatures fit on the higher end of what is expected based on the melting temperature of SmCo as discussed in Section 3.2.3 the compaction temperature often lies within 1/3 - 2/3 of T_m (Kelvin). This behaviour can be explained by the effect of the hydrogen and 5% nitrogen carrier gases on the oxidation of the particles. A higher compaction temperature for the nitrogen mixture suggests there is more oxidation than the 5% hydrogen because oxides are known to be difficult to compact than pure metals due to their higher melting temperature and lower solid state diffusivities [32]. Most metals undergo oxidation in the air which impedes the compaction process. From Figure 5.2 we believe that the SmCo nanoparticles produced in inert nitrogen are still oxidised by low levels of oxygen present during the particle formation. Furthermore, from the results it appears that the hydrogen carrier gas partially reduces the SmCo particles preventing the formation of oxide particles. The presence of oxides can be reduced further by using a higher concentration mixture of hydrogen such as 10% - 20% or

using a stronger reducing agent. However, higher mixtures come with safety concerns due to the flammability of hydrogen. The production of compacted SmCo nanoparticles shows clear benefits when generated using a mixture of hydrogen as the carrier gas. There are strong indications that oxidation is reduced resulting in a lower compaction temperature and allowing the formation of particles with a slightly lower mobility diameter.

5.1.3 SEM images

A DMA measures the mobility diameter, but this is not the same as the geometric diameter. For spherical, singly charged particles the mobility diameter is equal to the geometric diameter. However, the particles cannot be assumed to be spherical at all temperatures, so an SEM is used to investigate the morphology of the particles. Images of the surface provide complementary information to the compaction scan to give insight into how the particles reshape. SEM images of individual particles allow the morphology of the particles at different temperatures to be examined and the geometric diameter can be compared to the mobility diameter measured with the DMA. SmCo particles are deposited onto Si for 5 minutes using a typical accelerating voltage of 8 kV at different temperatures corresponding to key points in the compaction curve. Figure 5.3 shows SEM images of SmCo particles taken at different furnace temperatures using nitrogen. The geometric size of an "average" particle is estimated by the red arrow in the inset particle image. Figure 5.4 shows SEM images of particles produced with carrier gases of pure nitrogen and 5% hydrogen to investigate the effects of different gas conditions on particles morphology.

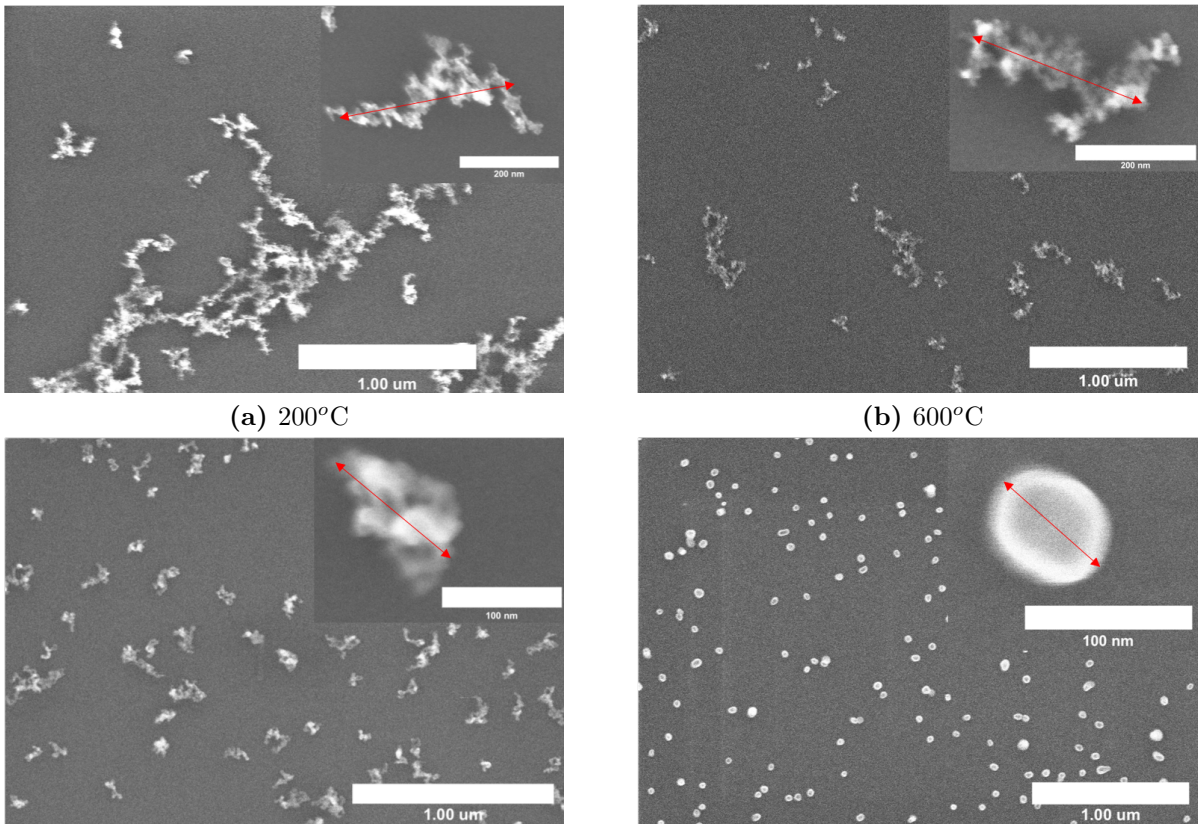

(a) 200^{o}C **(b)** 600^{o}C

(c) 800^{o}C **(d)** 1000^{o}C

Figure 5.3: SEM images of surface SmCo nanoparticles with inset single particles at increasing temperatures (a-d) from 200^{o}C to 1000^{o}C with nitrogen carrier gas.

Figure 5.3 (a, b) the images show that the particles are still agglomerates at temperatures below 600^{o}C because they display a fractal-like morphology with large estimations of 342 and 297 nm for the geometric size at 400^{o}C and 600^{o}C. Observing the compaction temperature in Figure 5.2 shows only a minor decrease in mobility over this temperature interval. Agglomerate particles visible below 600^{o}C is a high temperature compared to other materials such as Co [38] where agglomerates are present below 400^{o}C. Figure 5.3 (c, d) shows that the particles beginning to compact. In (c) at 800^{o}C the particles display a more compacted morphology with a large decrease in estimated geometric size of 125 nm which corresponds to a sharp decrease in mobility diameter. (d) at 1000^{o}C shows fully compacted particles, the particles have a uniform, spherical morphology. The geometric size is estimated at 75 nm another large decrease from the size at 800^{o}C. The compaction observed between 800^{o}C and 1000^{o}C is in agreement with the compaction temperature of 900^{o}C determined from the curve in Figure 5.2.

Figure 5.4 shows a comparison of SmCo particles produced from nitrogen and 5% hydrogen carrier gases at the same temperature of 600^{o}C. The SEM images are compared to investigate the differences in particle morphology. 600^{o}C is selected as the compaction curve in Figure 5.2 shows the largest difference in mobility diameter between the carrier gases at this temperature.

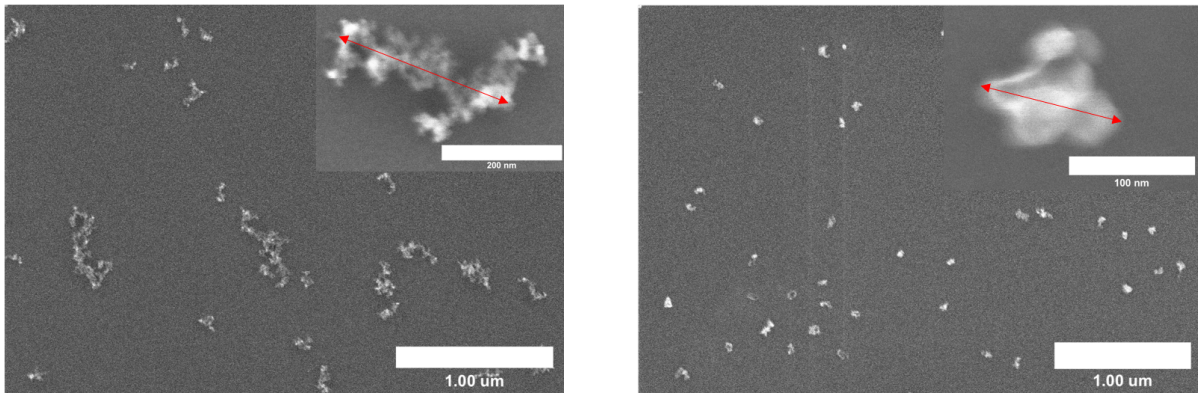

(a) Nitrogen **(b)** Nitrogen with 5% hydrogen

Figure 5.4: SEM images of SmCo nanoparticles on the surface with inset single particle at 600^{o}C for (a) pure nitrogen carrier gas and (b) Nitrogen with 5% hydrogen

Figure 5.4 (a) shows an agglomerate particle with a fractal, disorderly morphology with a geometric size 297 nm. However, Figure 5.4 (b) shows particles with more uniform, spherical particles that are more compact than at the equivalent temperature for nitrogen. The estimation of the geometric size is 112 nm which is smaller than the particles produced with nitrogen and closer in size to particles produced at 800^{o}C with nitrogen. This is in agreement with the compaction curve which suggests that particles produced with a hydrogen mixture begin to compact at a lower temperature compared to nitrogen.

5.1.4 Thermal charging

Spark discharge generation produces a large number of ions which cause the agglomerates to obtain unpredictable amounts of charge. The neutraliser shown in Figure 3.3 gives the particles a known charge distribution. However, at certain temperatures additional peaks corresponding to larger negative charges appear at lower electrical mobilities as described

by equation 2.5. The thermal charging is detrimental to nanoparticle analysis as discussed in section 3.2.4. The temperature range at which the thermal charges occur is recorded in Figure 5.5 with each scan offset in height for clarity.

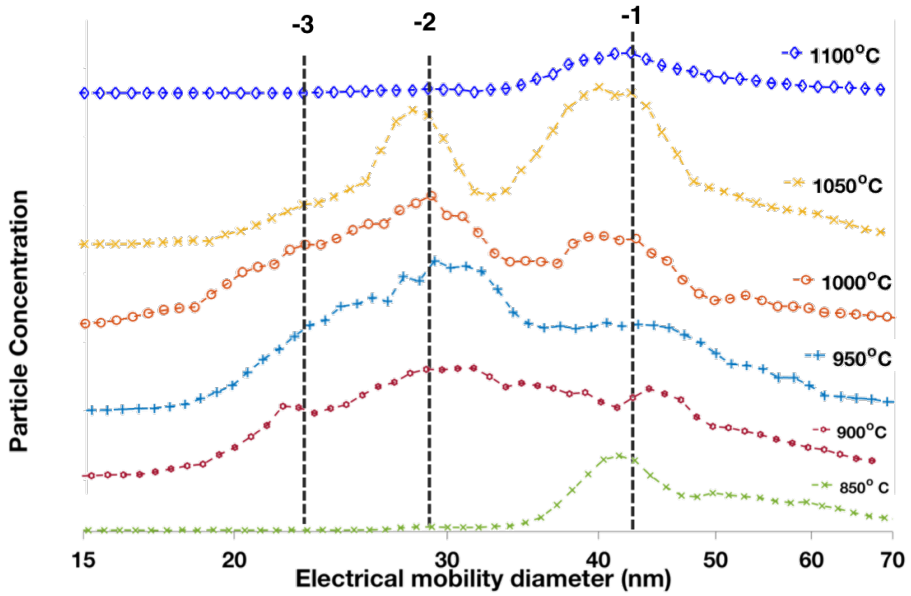

Figure 5.5: Thermal charging for SmCo nanoparticles produced from alloyed SmCo at a temperature range of 850^{o}C to 1100^{o}C using nitrogen carrier gas.

Figure 5.5 demonstrates how the multiple charges obscure the -1 peak which is the peak used to compare particles across temperatures. At 850^{o}C the peak is prominent and easily identified however, at a temperature of 950^{o}C, the singly charged peak becomes lost in the convulsion of multiply charged peaks that appear at lower mobility diameters. This makes the analysis of the scans at 950^{o}C and 1000^{o}C difficult due to possible mis-identification of the -1 peak which could change the compaction curve. At 1050^{o}C the -1 peak becomes clearly identifiable again and the thermal charging is completely gone at 1100^{o}C. This phenomenon has been identified before in other materials so is not unexpected [14] [33]. The thermal charging has not been investigated in detail and no satisfactory explanation has been offered. The thermal charging is temperature dependent which suggests that a source of electrons in the furnace interacts with the particles only at an interval of temperatures. Candidates for the source of electrons are the particles, carrier gas or the furnace wall however due to the relevant ionisation energies none of the sources appears to be good candidates for the source of electrons [33]. The cause of thermal charging is still an open question and more research is needed to fully understand the phenomenon.

5.1.5 Nanoparticle composition

A strength of spark discharge generation is the ability to mix different elements on the atomic level into bimetallic alloyed nanoparticle as discussed in section 3.2.2. To investigate if the mixing is successful from alloyed SmCo electrodes TEM was performed which measures the elemental composition of nanoparticles and can also provide a mapping of where each element is situated in a nanoparticle. Figure 5.6 shows a TEM image of a SmCo nanoparticle compacted at 1100^{o}C with nitrogen and with overlaid EDX mapping. Table 5.1 shows the normalised elemental distribution at different points in a particle. The TEM and EDX measurements were made by Calle Preger.

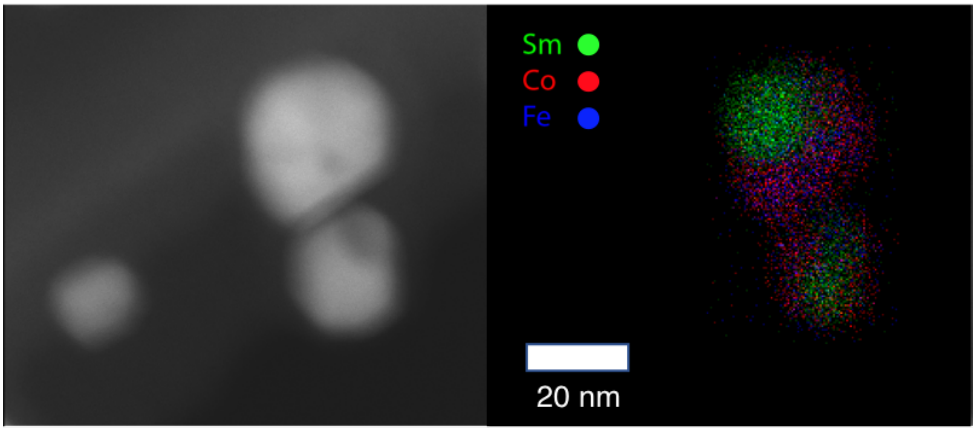

Figure 5.6: TEM and EDX measurements of compacted SmCo nanoparticles from alloyed SmCo electrodes with nitrogen. (Left) TEM of particles (Right) TEM with EDX mapping.

Table 5.1: EDX data of element composition in atomic% for particle 19 and particle 20.

Particle	Sm	Co	O	Fe
19.1	11.06	15.17	66.67	5.76
19.2	12.84	15.12	64.21	6.37
19.3	16.93	24.63	48.60	9.38
19.4	14.12	17.70	59.48	7.95
20.1	10.03	15.07	68.62	5.04
20.2	12.16	22.49	53.03	6.58
20.3	12.35	23.87	51.87	8.43
20.4	15.28	19.08	51.52	8.51

Table 5.1 shows that the nanoparticles produced from the alloyed SmCo contain some Fe impurities and also quite a high amount of oxygen in atomic percent. The ratio of Sm and Co is consistent within each particle, indicating that the mixing is good. The two common ratios of SmCo cobalt magnets are $SmCo_5$ and Sm_2Co_{17} as discussed in section 2.4.1, these correspond to a normalised atomic percent ratio of 17:83 and 11:89. Comparing the average ratio of Sm:Co for particle 19 gives 43:57 and for particle 20 38:62 these ratios are far from the ratios of Sm and Co used in SmCo magnet composition, with both measured particles having relatively more Sm. Across all 20 particles the average ratio is 40:60. However, from these limited statistics the particles appear to be well mixed and show potential that the SmCo nanoparticles could display magnetic properties.

5.2 Pure Samarium and Cobalt electrodes

SmCo nanoparticles were generated from two pure electrodes one of Sm and one of Co. The parameters of the electrode gap and driver voltage were maintained at 2 mm and 10 kV since these parameters produced particles with suitable properties for analysis. Maintaining the parameters allows for easier comparison between electrode types. As discussed in section 3.2.2 the position of the electrodes affects the composition of the nanoparticles with more material being contributed from the electrode acting as the cathode. To

investigate the effect of the electrodes position on the composition, morphology and compaction of the particles two configurations of the pure Sm and Co electrodes were tested. The two configurations will be referred to as *Sm and Co* where Sm acts as the cathode electrode and *Co and Sm* where Co acts as the cathode electrode.

5.2.1 Driver current

The size distribution of the SmCo particles from pure Sm and Co electrodes was investigated using driver currents 1 - 20 mA. The size distribution of the agglomerate particles was measured by scanning the first DMA at room temperature. The compacted particles were examined by scanning the second DMA after the furnace which was set at 1000^{o}C. In Figure 5.7 the size distribution of the particles at RT and 1000^{o}C is presented.

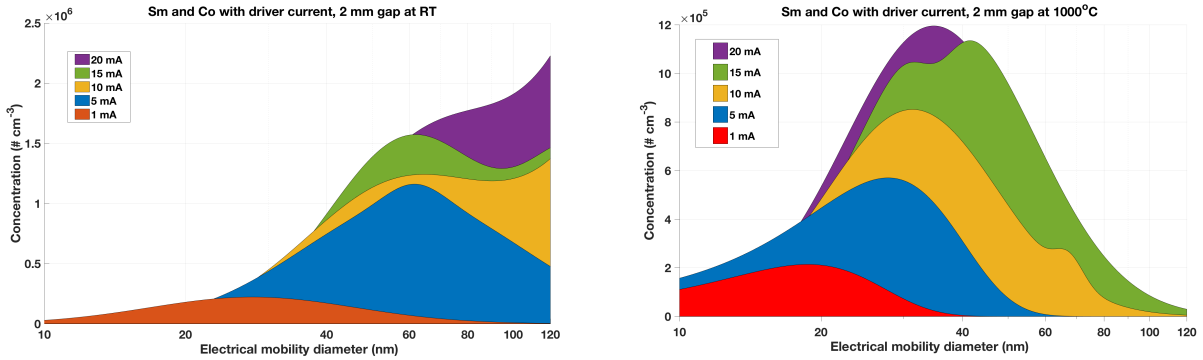

(a) RT **(b)** 1000^{o}C

Figure 5.7: Plot of the size distribution of particles produced from pure Sm and Co electrodes as the driver current is increased at temperatures of (a) RT and (b) 1000^{o}C.

In Figure 5.7 (a) the behaviour of an increase in the number concentration of particles and a shift in the size distribution is observed in agreement with Figure 5.1 and other materials. Similar to the SmCo electrodes if small particles below 20 nm need to be produced a low driver current of 1 mA is required. However, if larger particles are desired over 80 nm then a high driver current of over 10 mA should be selected. A difference between the production sources of SmCo in Figure 5.1 and pure Sm and Co in Figure 5.7 occurs at the larger currents of 10, 15 and 20 mA. The pure electrodes produce high concentrations of large particles, peaking off the scan at over 120 nm. The alloyed SmCo electrode at 10 mA peak in concentration at 85 nm. This aspect may be explained by increased coagulation of the particles produced from the pure Sm and Co electrodes then from alloyed SmCo. A possible reason for this is that the particles from the alloyed SmCo particles have more impurities such as Fe and Zn resulting in a lower limit for the amount of coagulation that can occur. The pure electrode particles could coalesce into larger agglomerates more easily than the particles from the alloyed electrodes.

5.2.2 Compaction

The compaction of the SmCo particles from the pure Sm and Co electrodes in both configurations was examined using both carrier gases of pure nitrogen and nitrogen with 5% hydrogen. Figure 5.8 (a) shows the compaction curve for the *Sm and Co* configuration with both gases and (b) shows the compaction curve for the *Co and Sm* configuration again with both gases.

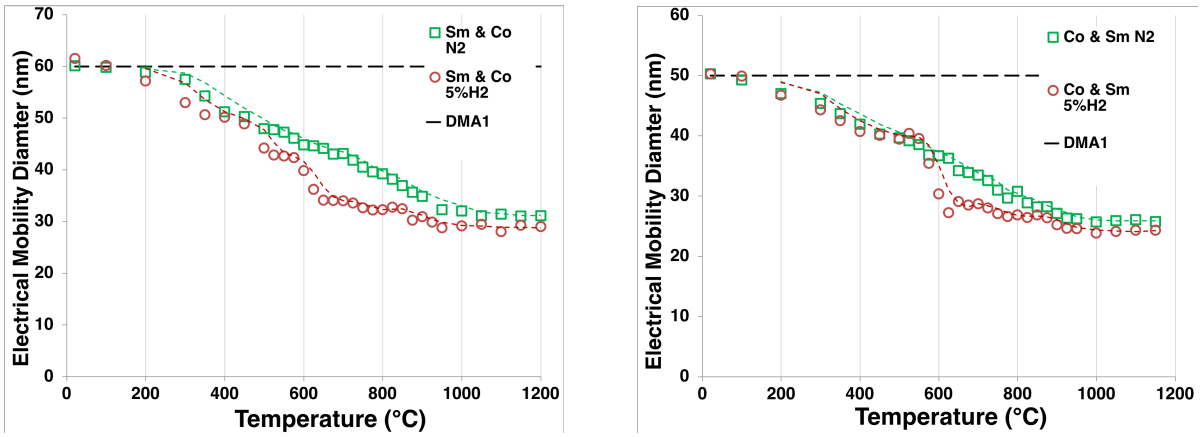

(a) Sm and Co **(b)** Co and Sm

Figure 5.8: Compaction curves of SmCo nanoparticles with mobility diameter against temperature using carrier gases of nitrogen and 5% hydrogen. The dashed lines indicate a 3 point moving average trendline with configurations (a) Sm and Co and (b) Co and Sm

Figure 5.8 (a) and (b) show that the nanoparticles compact gradually over the temperature range when using pure nitrogen as the carrier gas. In (a) a mobility diameter of 31 nm is reached above the compaction temperature of 900^{o}C. In (b) mobility of 26 nm is reached above a similar compaction temperature of 875^{o}C. The compaction curves using pure nitrogen in (a) and (b) are very similar to the consistent gradual decrease in mobility observed from alloyed SmCo electrodes with nitrogen in Figure 5.2. The compaction temperatures again fall within the upper range of 1/3 - 2/3 T_m in Kelvin. The compaction curves using 5 % hydrogen in Figure 5.8 (a) and (b) show a faster decrease in mobility diameter compared to nitrogen creating a lower curve. This behaviour is expected and is in agreement with the measurements from the alloyed SmCo electrodes. (a) and (b) reach slightly lower mobility diameters of 28 nm and 24 nm at temperatures above their T_c of 725^{o}C and 750^{o}C respectively. This aspect is again similar to that observed for the alloyed SmCo electrodes with nitrogen gas. However, there is a difference in the curves as the temperature at which the mobility begins to decrease faster is shifted higher for the pure Sm and Co electrodes in both configurations. This gives the compaction curves from pure Sm and Co similar shapes for both 5 % hydrogen and nitrogen. A possible explanation for this is due to the pure electrodes not containing impurities such as Cu or Zn. The elements Zn and Cu both have lower melting temperatures than Co which may allow the particles produced from the alloyed SmCo electrodes to compact at lower temperatures than the pure Sm and Co electrodes. Another potential explanation is that the 5 % hydrogen gas is less effective as a reducing agent for pure Sm and Co and thus more of the particles become oxidised. Oxidised particles have higher melting temperatures and hence the curve would be shifted closer to the nitrogen curve.

5.2.3 SEM images of pure Sm and Co

SEM images were taken to complement the compaction curve to gain further understanding of how the particles reshape in the tube furnace. The SmCo particles were deposited onto Si substrates for 5 minutes using an accelerating voltage of 8 kV. Figure 5.9 shows the SEM images of particles produced from the Sm and Co configuration with nitrogen, at increasing furnace temperatures. The geometric size is a rough estimation using an overlaid red arrow on what is deemed to be an ”average” particle at the temperature.

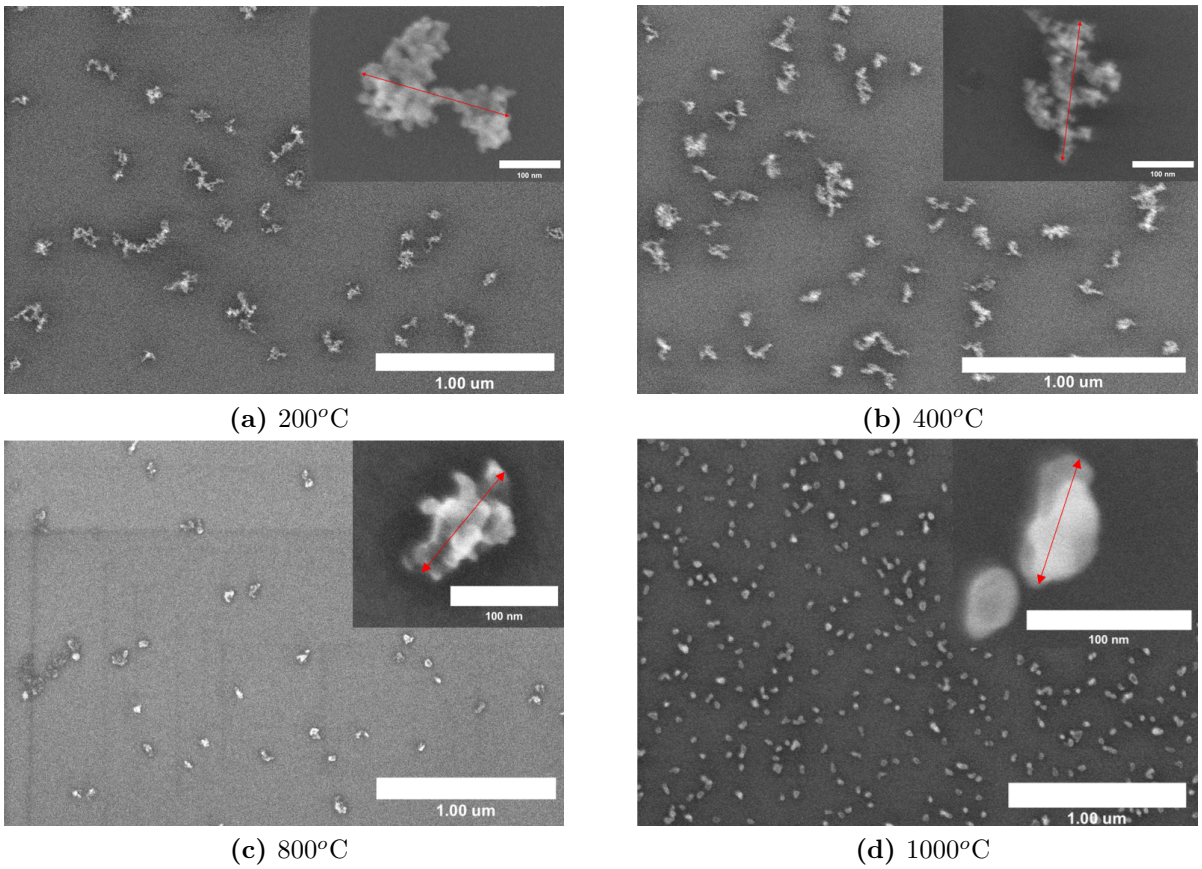

(a) 200^{o}C **(b)** 400^{o}C

(c) 800^{o}C **(d)** 1000^{o}C

Figure 5.9: SEM images of surface SmCo nanoparticles from Sm and Co electrodes with inset single particle with measured size. Images (a-d) show increasing temperatures from 200^{o}C to 1000^{o}C with nitrogen carrier gas.

Figure 5.9 (a, b) show that the compaction is negligible below 400^{o}C and the particles are still agglomerates. The geometric sizes are estimated to be large at 246 nm and 220 nm for 200^{o}C and 400^{o}C. This is in agreement with the compaction curve which shows a steady decrease in mobility diameter in the same temperature interval. Figure 5.9 (c) shows particles on the surface that are more compacted at 800^{o}C than the alloyed electrodes in Figure 5.3 (c). The estimated geometric size is similar at 119 nm and 125 nm however since these are only taken for one particle they can be ignored. Figure 5.3 (d) the particles are beyond the compaction temperature of 900^{o}C however they appear not to be fully compacted. The particles display a shard shaped morphology and the geometric size is estimated at 81 nm larger than the particles from the alloyed SmCo electrode. This is in disagreement with the compaction curve which indicates that the particles should be fully compacted. A reason for this may be due to the shard morphology of the nanoparticles which are comparatively thinner compared to spherical particles. This may cause the DMA to underestimate the mobility diameter. A deposition at a higher temperature could be performed to investigate if the compacted particle morphology is shard like or if the particles haven't been fully compacted. The compaction and SEM images indicate that if spherical particles are desired then alloyed SmCo electrodes are the preferred production method for SmCo nanoparticles.

Figure 5.10 shows particles produced from pure Sm and Co electrodes using different carrier gases to examine the morphology of the nanoparticles under different conditions.

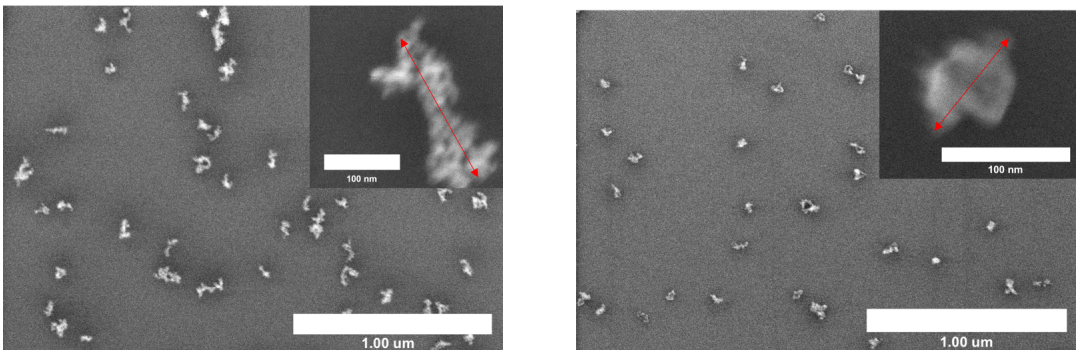

(a) Nitrogen **(b)** Nitrogen with 5% hydrogen

Figure 5.10: SEM images of surface SmCo particles from pure Sm and Co electrodes with a single particle and measured size at 600^{o}C. Images (a) nitrogen and (b) 5% hydrogen.

Figure 5.10 shows that the 5% hydrogen reduces the amount of oxidation resulting in the particles compacting at a lower temperature. This is a similar result compared to changing the carrier gases for alloyed SmCo electrodes in Figure 5.4. Figure 5.10 (a) shows the oxidised particles are larger in size and have compacted less compared to (b). There is a large difference in estimated geometric size from 206 nm to 91 nm. This behaviour is due to the melting temperature of oxides being higher causing the particles to require a higher temperature to compact with nitrogen.

SEM images were taken for the second Co and Sm position of the electrodes to investigate how the cathode material effects the morphology of the particles. Figure 5.11 shows SEM images for the particles taken at increasing temperatures with estimated geometric size.

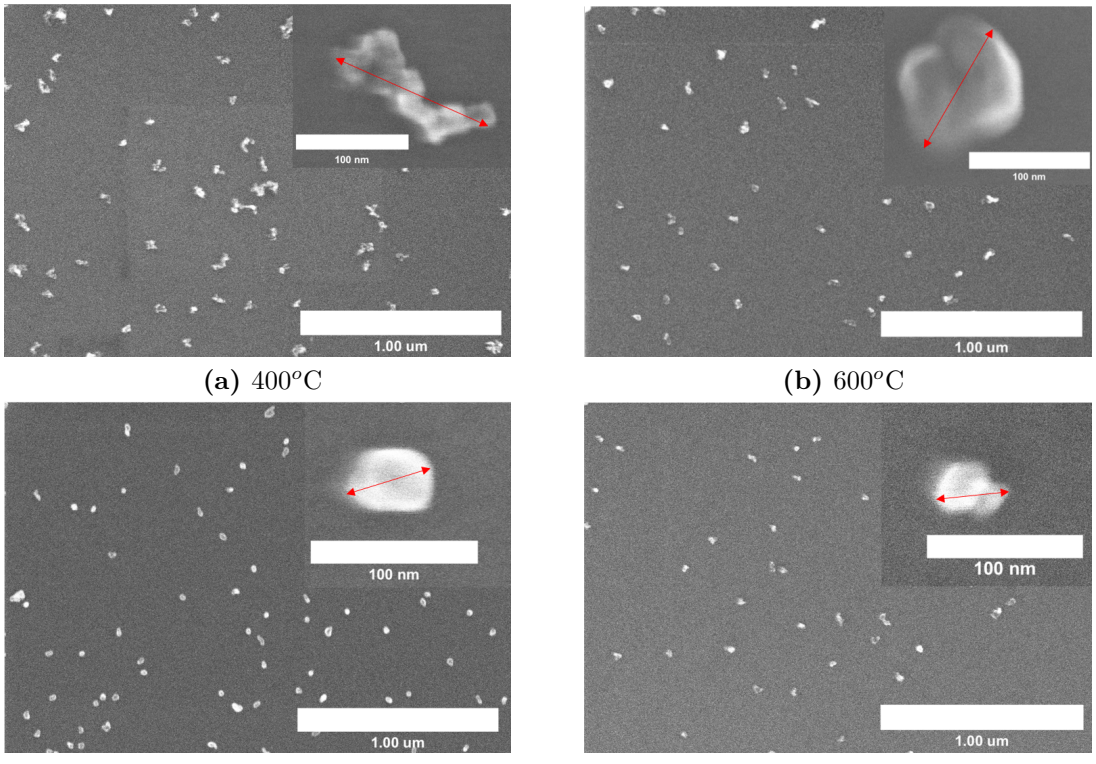

(a) 400^{o}C **(b)** 600^{o}C

(c) 800^{o}C **(d)** 1000^{o}C

Figure 5.11: SEM images of surface SmCo particles from pure Co and Sm electrodes with particle and size. Images (a-d) show increasing temperatures from 400^{o}C to 1000^{o}C with nitrogen.

Figure 5.11 (a) at 400^{o}C shows that the particles are still agglomerates with large fractal structures. Comparing to the surface particles in Figure 5.9 (b) shows that pure Co and Sm particles appear to be more compacted. This trend continues in Figure 5.11 (b) which show quite well-compacted particles with an estimated geometric diameter of 116 nm. (c) at 800^{o}C shows what appears to be nearly completely compacted particles with a small estimated geometric size of 60 nm. The compaction curve in Figure 5.8 (b) shows that the mobility diameters decrease at nearly a constant rate from 400^{o}C to 800^{o}C which is reflected in the consistent decreases in estimated geometric size. Figure 5.9 (d) show compacted, spherical particles of estimated geometric size 52 nm at a temperature beyond the T_c of 875^{o}C. The Co and Sm electrode particles are smaller compared to the SmCo electrode particles shown in Figure 5.9 (d). If SmCo nanoparticles with the smallest size are required, then pure electrode of Co and Sm are the best production source.

Figure 5.12 examines how different gas conditions affects the morphology of the particles produced from pure Co and Sm using the different carrier gases.

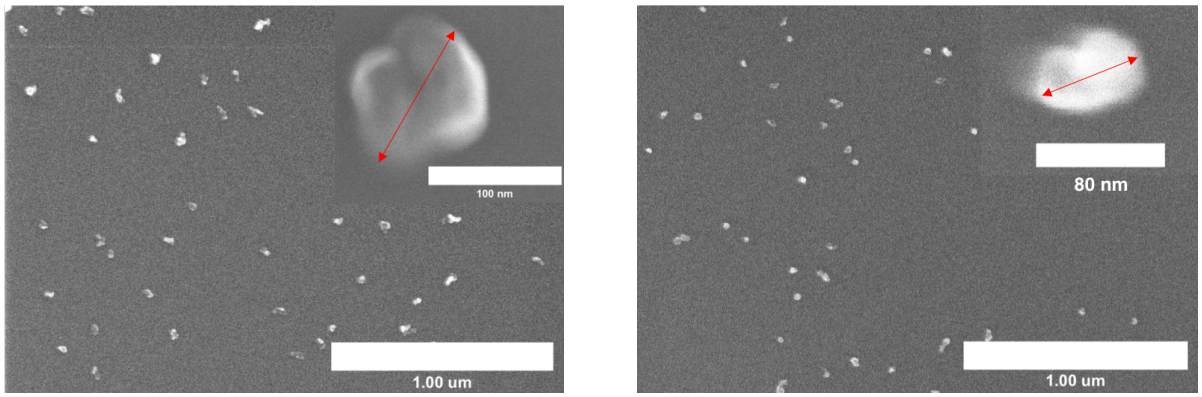

(a) Nitrogen **(b)** Nitrogen with 5% hydrogen

Figure 5.12: SEM images of surface SmCo particles from pure Co and Sm electrodes with a single particle and measured size at 600^{o}C with carrier gases (a) nitrogen and (b) 5% hydrogen.

Figure 5.12 shows the particles are more compacted with a smaller geometric size when 5% hydrogen carrier is used. This is the expected behaviour since hydrogen reduces the oxidation of particles. The discrepancy is that the difference in size between the particles is not as dramatic as with alloyed SmCo and pure Sm and Co electrodes. The particles from nitrogen have a geometric size of 116 nm and from 5% hydrogen are estimated as 74 nm. Inspecting the compaction curve in Figure 5.8 (b) shows that the particles have similar mobility diameters at 600^{o}C, closer than the other production types.

5.2.4 Thermal Charging

Significant thermal charging was again observed for the nanoparticles produced from the pure Sm and Co electrodes. Figure 5.13 shows the thermal charges using the pure Sm and Co electrodes with 5% hydrogen carrier gas which are offset in height for clarity.

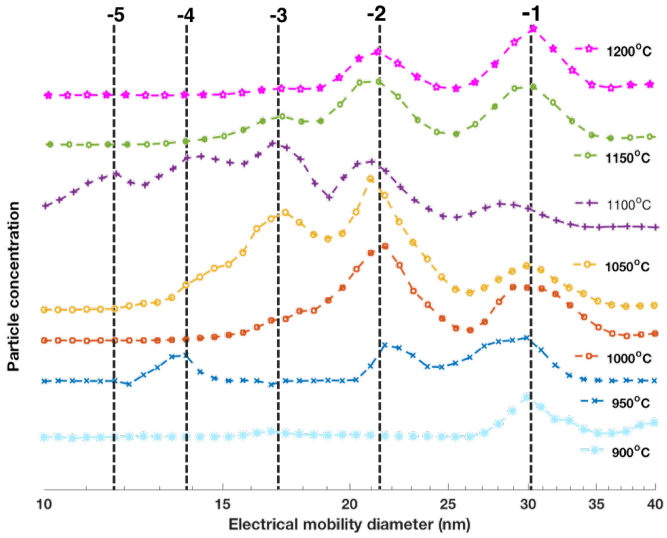

Figure 5.13: Thermal charging of SmCo particles from pure Sm and Co using 5% H2.

In Figure 5.13 large charges up to -5 are observed obscuring the -1 peak from 1000^{o}C to 1100^{o}C. This is similar to the range of temperatures observed for the alloyed SmCo electrodes in Figure 5.5. The similar temperature range would suggest that the source of the particles is independent of the electrode material. Thermal charging has been observed for materials such as Au at a similar temperature of 950^{o}C to 1100^{o}C. I believe that the most likely source of the electrons is from the furnace since the thermal charges become visible when particles are heated in a system that heats via a tube furnace.

5.2.5 Nanoparticle composition

How well the SmCo nanoparticles produced from the pure Co and Sm electrodes mixed was investigated by taking TEM and EDX measurements at 1000^{o}C with nitrogen. Figure 5.14 (a) shows a TEM image of a SmCo nanoparticle and the location of the corresponding spectrum in Table 5.2 of Sm, Co and O in atomic %. (b) shows the TEM image with overlaid EDX measurements to give a mapping of the elements. The data was measured by Maria Messing.

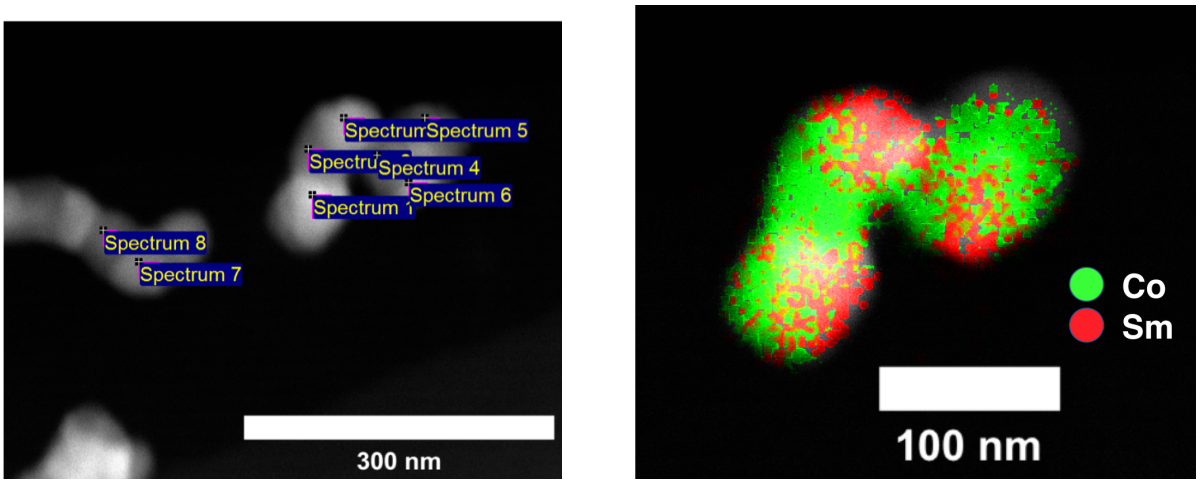

(a) TEM **(b)** TEM with EDX mapping

Figure 5.14: TEM and EDX measurements of compacted SmCo nanoparticles from Co and Sm electrodes with nitrogen. (a) TEM image with probe locations (b) TEM with EDX mapping.

Table 5.2: EDX data of element composition in atomic % at each spectrum's location.

Spectrum	Sm	Co	O
1	18.90	19.62	61.48
2	1.60	37.65	60.75
3	21.56	8.55	69.89
4	6.79	31.50	61.71
5	1.01	35.58	63.41
6	24.32	14.21	61.47
7	20.72	18.13	61.15
8	1.06	35.98	62.96

Figure 5.14 (b) the elemental mapping displays regions of the particle rich in Co and other regions rich in Sm. This is further reflected in Table 5.2 when O is removed and the relative atomic % ratio is found of Sm:Co, spectrum point 2 has a ratio of 4:96 and at point 3 72:28. These points are taken next to each other on the particle but have very different elemental compositions, this indicates that the SmCo particles are phase separated and the mixing of the elements is poor. The data is in agreement with the observation that the cathode electrode contributes more material to the particles since points 2,5 and 8 have large ratios of Co and at no point does Sm have such a large ratio. The two common ratios of SmCo cobalt magnets are $SmCo_5$ and Sm_2Co_{17} which correspond to a normalised atomic % ratio of 17:83 and 11:89. However comparing these values to the EDX data is frivolous since the range of the composition varies drastically. This is in contrast to the SmCo particles produced from the alloyed electrodes in Table 5.1 which showed more consistent mixing. From the results the limited statistics of the TEM and EDX data it would suggest that these nanoparticles are not well mixed and are unlikely candidates for nanoparticles with magnetic behaviour. From the EDX data on particles produced with hydrogen (not shown) the oxygen level is lower indicating less oxidised particles which are in good agreement with the compaction curves displayed in Figure 5.2 5.8 and the behaviour of other materials such as Sn, Co and Bi [38].

Chapter 6

Outlook and Conclusion

The goal of pressing electrodes from samarium and cobalt powder was ultimately unsuccessful however the pressing of stainless steel powder showed great promise. Electrodes were pressed and successfully withstood the energy of the spark in the spark discharge generator. This is a positive sign that with the correct tool samarium-cobalt electrodes could be manufactured and used in the SDG. Both the cylinder and block pressing tools were flawed but I believe that a combination of the two would be the best way forward to press electrodes. Combining the sealed cylinder design with the increased plunger rigidity of the second block tool. The material that the tool chamber is made from should also be given special attention to, in order to ensure that the powder cannot become impacted and pressed into the tools chamber. However, despite these setbacks I believe that the potential is there to manufacture custom electrodes from powdered material.

Nanoparticles of samarium-cobalt were generated successfully using the SDG. The SDG is a powerful tool that allowed for great control and flexibility with tuning the size distribution of the nanoparticles. Changing the driver current allows the size distribution of the particles to be shifted and when combined with the tandem DMA allowed for good control over the size of particles that were deposited. The tube furnace compacts the nanoparticles well to generate particles with a favourable, spherical morphology. The mixing capabilities of the SDG were analysed with the TEM and EDX and showed SmCo nanoparticles that had been mixed but mixed inconsistently.

The three different production methods of SmCo nanoparticles all had advantages and disadvantages. The pure Sm and Co electrode configuration produced small SmCo nanoparticles but also particles with a shard like morphology. The Co and Sm configuration improved on this by obtaining the smallest nanoparticle sizes recorded and also maintained a more uniform, spherical morphology. However, from the compositional analysis the SmCo particles appear to be phase separated and not well mixed. On the contrary, the alloyed SmCo electrodes appeared to have the best mixing of Sm and Co and also had a desirable spherical morphology. For these reasons I believe that the alloyed SmCo electrodes are the best candidate production type of electrodes for SmCo nanoparticles.

Looking to the future a third tool should be produced to press SmCo electrodes so that they can be analysed and compared with the other production electrodes. The potentially magnetic properties of the SmCo particles should also be investigated by testing if it is possible to magnetise SmCo and create magnetic nanoparticles.

The potentials for custom made nanoparticles are huge. Nanoparticles have enormous potential and that potential is beginning to become realised with the introduction of nanoparticles into mainstream commercial applications in medicine, electronics and chemistry. Harnessing magnetic nanoparticles for cancer treatment are being researched and in the future all of humankind will benefit from particles invisible to the naked eye.

Bibliography

[1] Szu-Hung Chen et al. "High-performance III-V MOSFET with nano-stacked high-k gate dielectric and 3D fin-shaped structure". In: *Nanoscale Research Letters* 7.1 (Aug. 2012), p. 431. URL: https://doi.org/10.1186/1556-276X-7-431.

[2] Ian Sofian Yunus et al. "Nanotechnologies in water and air pollution treatment". In: *Environmental Technology Reviews* 1.1 (2012), pp. 136–148.

[3] Science daily. *Nanoparticle*. Accessed: 2019-04-30. URL: https://www.sciencedaily.com/terms/nanoparticle.htm.

[4] Benedette Cuffari. *What Nanomaterials Exist in Nature?* 2018. URL: https://www.azonano.com/article.aspx?ArticleID=4837.

[5] C.D. Jones M.O. Andreae and P. M. Cox. "Strong present-day aerosol cooling implies a hot future". In: *Nature* 435 (2005), pp. 1187–1190.

[6] Zhu Y Zhao L and Chen Z. "Cardiopulmonary effects induced by occupational exposure to titanium dioxide nanoparticles". In: *Nanotoxicology* 12(2) (2018), pp. 169–184.

[7] W. C. Hinds. *Aerosol Technology: Properties, Behavior, and Measurement of Airborne Particles, 2nd Edition*. John Wiley and Sons, INC, 1999.

[8] Bengt O. Meuller et al. "Review of Spark Discharge Generators for Production of Nanoparticle Aerosols". In: *Aerosol Science and Technology* 46.11 (2012), pp. 1256–1270. URL: https://doi.org/10.1080/02786826.2012.705448.

[9] H. et al. Kim. "Parallel patterning of nanoparticles via electrodynamic focusing of charged aerosols". In: *National Nanotechnology* 1 (2006), pp. 117–121.

[10] Rachel Wallach. *With new technique, researchers create metallic alloy nanoparticles with unprecedented chemical capabilities*. Accessed: 2019-03-30. URL: https://hub.jhu.edu/2018/04/04/new-nanoparticle-metallic-alloys/.

[11] Yonggang Yao et al. "Carbothermal shock synthesis of high-entropy-alloy nanoparticles". In: *Science* 359.6383 (2018), pp. 1489–1494. URL: https://science.sciencemag.org/content/359/6383/1489.

[12] Hyangki Sung and Mansoo Choi. "Assembly of Nanoparticles: Towards Multiscale Three-Dimensional Architecturing". In: *KONA Powder and Particle Journal* 30 (2013), pp. 31–46.

[13] Jiri et al. Kudr. "Magnetic Nanoparticles: From Design and Synthesis to Real World Applications". In: *Nanomaterials* 7(9) (2017), p. 243.

[14] C. Preger. "Generation and Deposition of Magnetic Aerosol Nanoparticles". 2018.

[15] "Control of cerebral ischemia with magnetic nanoparticles". English. In: *Nature Methods* 14.1 (2017), pp. 160–166.

[16] M. Magnusson. "Metal and Semiconductor Nanocrystals for Quantum Devices". 2001.

[17] CD Bioparticle Products. *Properties and Applications of Magnetic Nanoparticles*. Accessed: 2019-05-01. URL: https://www.cd-bioparticles.com/t/Properties-and-Applications-of-Magnetic-Nanoparticles_55.html.

[18] Leena Mohammed et al. "Magnetic nanoparticles for environmental and biomedical applications: A review". In: *Particuology* 30 (2017), pp. 1–14. URL: http://www.sciencedirect.com/science/article/pii/S1674200116300852.

[19] Suying Yan et al. "Heat transfer property of SiO2/water nanofluid flow inside solar collector vacuum tubes". In: *Applied Thermal Engineering* 118 (2017), pp. 385–391. URL: http://www.sciencedirect.com/science/article/pii/S1359431117313054.

[20] Angl Apostolov, Iliana Apostolova, and Julia Wesselinowa. "Specific absorption rate in Zn-doted ferrites for self-controlled magnetic hyperthermia". In: *The European Physical Journal B* 92.3 (Apr. 2019), p. 58. URL: https://doi.org/10.1140/epjb/e2019-90567-2.

[21] Piao Xu et al. "Use of iron oxide nanomaterials in wastewater treatment: A review". In: *Science of The Total Environment* 424 (2012), pp. 1–10. URL: http://www.sciencedirect.com/science/article/pii/S0048969712001982.

[22] Diego Iglesias et al. "Catalytic applications of magnetic nanoparticles functionalized using iridium N-heterocyclic carbene complexes". In: *New J. Chem.* 39 (8 2015), pp. 6437–6444. URL: http://dx.doi.org/10.1039/C5NJ00803D.

[23] Hwang et al. Lee. "Synthesis of Samarium-Cobalt Sub-micron Fibers and Their Excellent Hard Magnetic Properties". In: *Frontiers in chemistry* 6(18) (2018).

[24] Advanced magnets. *Sintered SmCo magnets*. Accessed: 2019-03-30. URL: http://www.advancedmagnets.com/sintered-smco-magnets/.

[25] T.V. Pfeiffer, J. Feng, and A. Schmidt-Ott. "New developments in spark production of nanoparticles". In: *Advanced Powder Technology* 25.1 (2014), pp. 56–70. URL: http://www.sciencedirect.com/science/article/pii/S0921883113002446.

[26] First4magnets. *How are samarium cobalt magnets made?* Accessed: 2019-04-30. URL: https://www.first4magnets.com/tech-centre-i61/information-and-articles-i70/samarium-cobalt-magnet-information-i85/how-are-samarium-cobalt-magnets-made-i111.

[27] M. Messing. "Engineered Nanoparticles Generation, Characterization, and Applications". 2011.

[28] Linus Ludvigsson, Bengt O Meuller, and Maria E Messing. "Investigations of initial particle stages during spark discharge". In: *Journal of Physics D: Applied Physics* 48.31 (July 2015), p. 314012. URL: https://doi.org/10.1088%2F0022-3727%2F48%2F31%2F314012.

[29] N. S. Tabrizi et al. "Synthesis of mixed metallic nanoparticles by spark discharge". In: *Journal of Nanoparticle Research* 11.5 (Dec. 2008), p. 1209. URL: https://doi.org/10.1007/s11051-008-9568-8.

[30] N. S. Tabrizi et al. "Generation of nanoparticles by spark discharge". In: *Journal of Nanoparticle Research* 11.2 (May 2008), p. 315. URL: https://doi.org/10.1007/s11051-008-9407-y.

[31] Jicheng Feng et al. "Internally mixed nanoparticles from oscillatory spark ablation between electrodes of different materials". In: *Aerosol Science and Technology* 52.5 (2018), pp. 505–514. URL: https://doi.org/10.1080/02786826.2018.1427852.

[32] M. N. A. Karlsson et al. "Compaction of agglomerates of aerosol nanoparticles: A compilation of experimental data". In: *Journal of Nanoparticle Research* 7.1 (Feb. 2005), pp. 43–49. URL: https://doi.org/10.1007/s11051-004-7218-3.

[33] Martin H. Magnusson et al. "Gold Nanoparticles: Production, Reshaping, and Thermal Charging". In: *Journal of Nanoparticle Research* 1.2 (June 1999), pp. 243–251. URL: https://doi.org/10.1023/A:1010012802415.

[34] Nanoscience Instruments. *Scanning Electron Microscopy*. Accessed: 2019-04-30. URL: https://www.nanoscience.com/techniques/scanning-electron-microscopy/.

[35] Atlas steels. *Stainless Steel grade Datasheets*. Accessed: 2019-04-30. URL: http://www.worldstainless.org/Files/issf/non-image-files/PDF/Atlas_Grade_datasheet_-_all_datasheets_rev_Aug_2013.pdf.

[36] The Linde Group. *Sintering of steels*. Accessed: 2019-05-05. URL: http://www.linde-gas.com/en/legacy/attachment?files=tcm:s.17-460206,tcm:.17-460206,tcm:17-460206.

[37] Bengt O Meuller and Maria E Messing et al. "Generation of nanoparticle aerosols by spark discharge". In: *Aerosol Science and Technology* (2011).

[38] R. T. Hallberg et al. "Hydrogen-assisted spark discharge generated metal nanoparticles to prevent oxide formation". In: *Aerosol Science and Technology* 52.3 (2018), pp. 347–358. eprint: https://doi.org/10.1080/02786826.2017.1411580. URL: https://doi.org/10.1080/02786826.2017.1411580.

[39] Koichi Nakaso et al. "Evaluation of the change in the morphology of gold nanoparticles during sintering". In: *Journal of Aerosol Science* 33.7 (2002), pp. 1061–1074. URL: http://www.sciencedirect.com/science/article/pii/S0021850202000587.

Appendix

6.1 Compaction curves

Figure 6.1 shows the compaction comparing all the production methods using nitrogen.

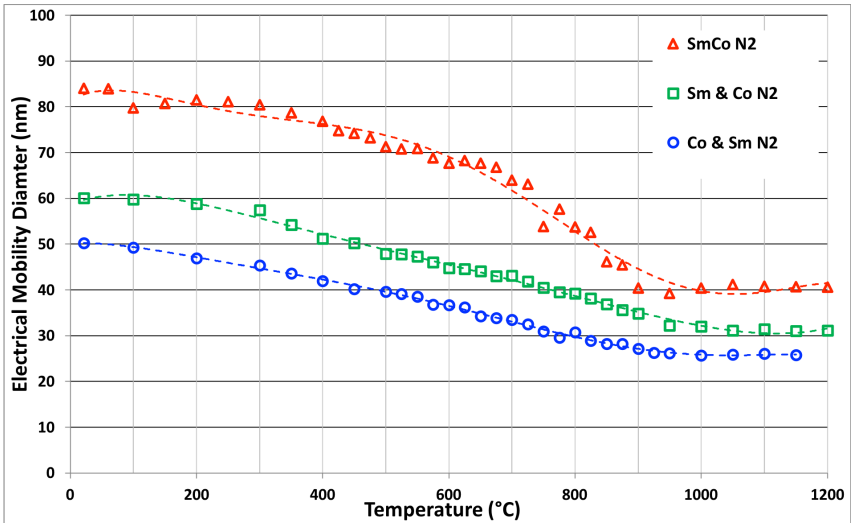

Figure 6.1: Compaction curve of SmCo particles with three production materials using nitrogen.

Figure 6.2 shows the compaction comparing all production methods using 5% hydrogen.

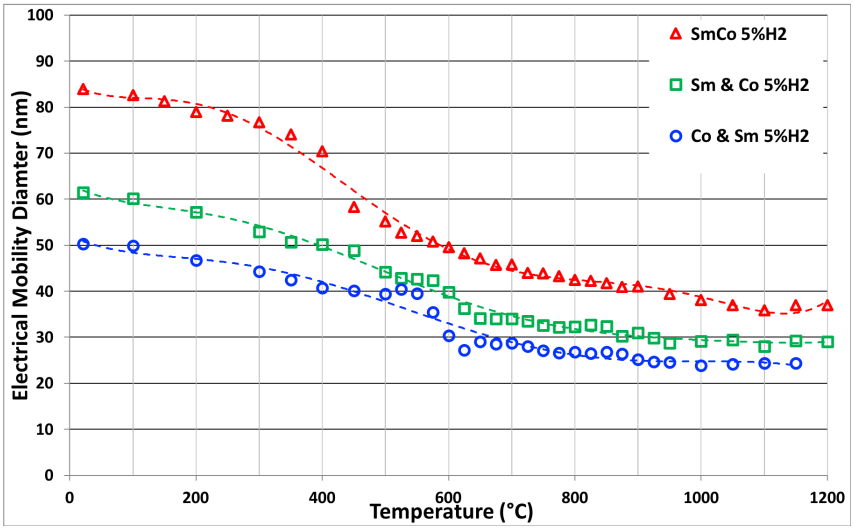

Figure 6.2: Compaction curve of SmCo particles with three production materials using 5% hydrogen.

Figure 6.3 is the compaction curve comparing the two positions of the pure Sm and Co electrodes using nitrogen carrier gas.

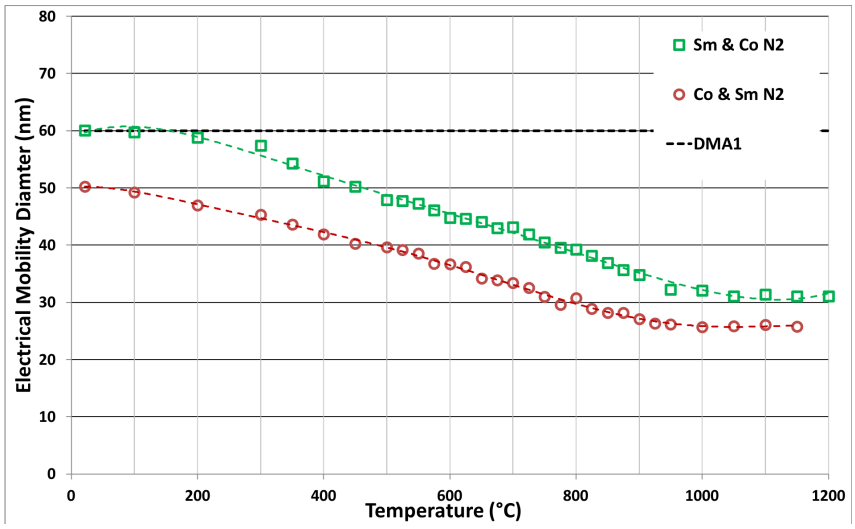

Figure 6.3: Compaction curve of samarium-cobalt nanoparticles comparing Sm and Co (Anode vs Cathode) production materials using nitrogen carrier gas.

6.2 Thermal charging

Figure 6.4 shows thermal charging from pure Sm and Co electrodes from which only -1, -2 and -3 charges are seen.

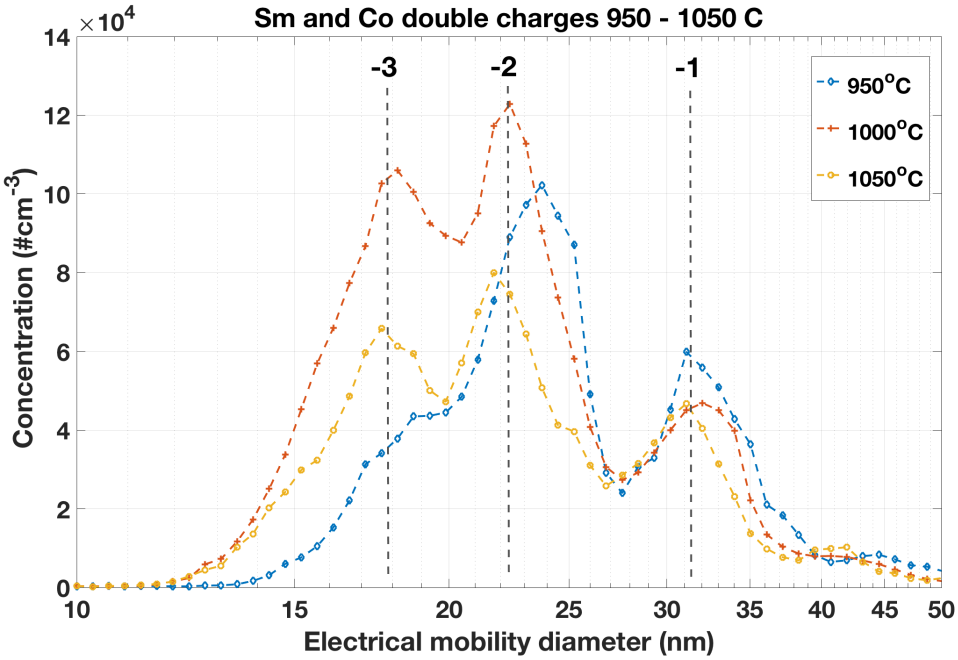

Figure 6.4: Thermal charging of SmCo particles using pure Sm and Co electrodes over at a temperature interval of 950^{o}C to 1050^{o}C using nitrogen carrier gas.

Figure 6.5 shows thermal charging from pure Co and Sm electrodes from which only -1, -2 and -3 charges are seen.

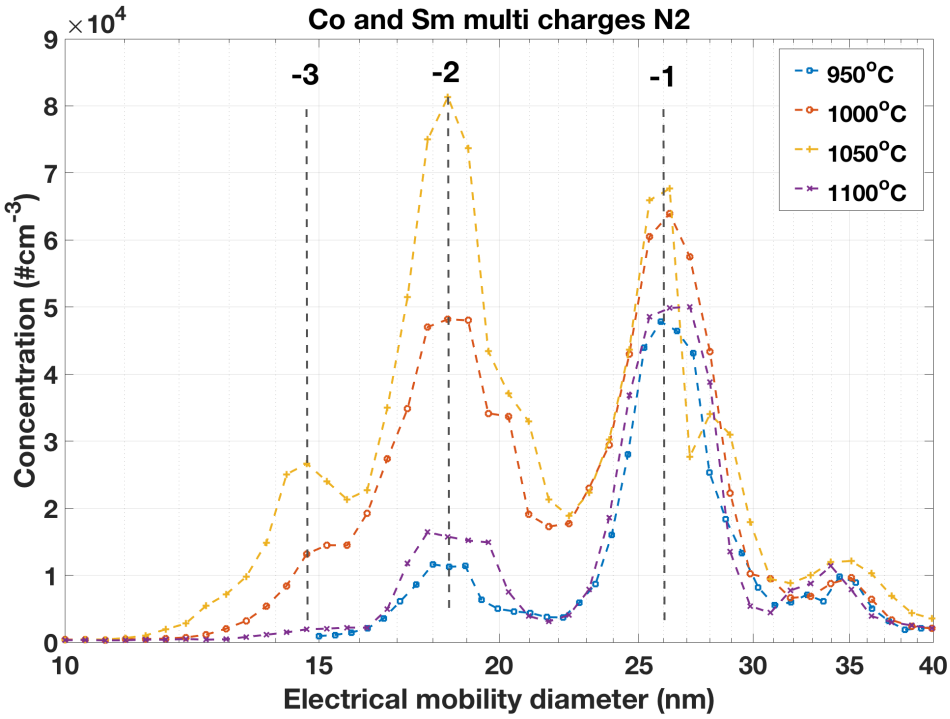

Figure 6.5: Thermal charging of SmCo particles using pure Co and Sm particles over at a temperature interval of 950^{o}C to 1050^{o}C using Nitrogen carrier gas.